Journal of the Mechanics and Physics of Solids 61 (2013) 1144–1167

Contents lists available at SciVerse ScienceDirect

Journal of the Mechanics and Physics of Solids

journal homepage: www.elsevier.com/locate/jmps

A generalized mechanical model for suture interfaces of arbitrary geometry

Yaning Li [a,b,c], Christine Ortiz [a], Mary C. Boyce [b,*]

[a] Department of Materials Science and Engineering, Massachusetts Institute of Technology, Cambridge, MA 02139, USA
[b] Department of Mechanical Engineering, Massachusetts Institute of Technology, Cambridge, MA 02139, USA
[c] Department of Mechanical Engineering, University of New Hampshire, Durham, NH 03824, USA

ARTICLE INFO

Article history:
Received 10 April 2012
Received in revised form
25 September 2012
Accepted 6 October 2012
Available online 5 December 2012

Keywords:
Suture
Interface
Stiffness
Strength
Fracture Toughness

ABSTRACT

Suture interfaces with a triangular wave form commonly found in nature have recently been shown to exhibit exceptional mechanical behavior, where geometric parameters such as amplitude, frequency, and hierarchy can be used to nonlinearly tailor and amplify mechanical properties. In this study, using the principle of complementary virtual work, we formulate a generalized, composite mechanical model for arbitrarily-shaped interdigitating suture interfaces in order to more broadly investigate the influence of wave-form geometry on load transmission, deformation mechanisms, anisotropy, and stiffness, strength, and toughness of the suture interface for tensile and shear loading conditions. The application of this suture interface model is exemplified for the case of the general trapezoidal wave-form. Expressions for the in-plane stiffness, strength and fracture toughness and failure mechanisms are derived as nonlinear functions of shape factor β (which characterizes the general trapezoidal shape as triangular, trapezoidal, rectangular or anti-trapezoidal), the wavelength/amplitude ratio, the interface width/wavelength ratio, and the stiffness and strength ratios of the skeletal/interfacial phases. These results provide guidelines for choosing and tailoring interface geometry to optimize the mechanical performance in resisting different loads. The presented model provides insights into the relation between the mechanical function and the morphological diversity of suture interface geometries observed in natural systems.

1. Introduction

A diversity of geometrically structured interfaces and joints is found in biology (Fig. 1), for example bone and armored exoskeletons (Ji and Gao, 2004; Gao, 2006; Barthelat et al., 2007; Tang et al., 2007; Song et al., 2010, Dunlop et al., 2011), the cranium (Pritchard et al., 1956; Persson et al., 1978; Hubbard et al., 1971; Jaslow, 1990; Herring, 2008), the turtle carapace (Krauss et al., 2009) and algae (Gebeshuber et al., 2003; Spaulding et al., 2009; Potapova and English, 2010; Garcia et al., 2011). In such systems, geometry is a key determinant of mechanical and biological functions such as growth, respiration, locomotion, penetration resistance, load transmission, and energy absorption (Pritchard et al., 1956; Jaslow, 1990; Herring, 2008; Dunlop et al., 2011). For example, the roles of the dove-tailed thickness profile of the platelets

* Corresponding author.
E-mail address: mboyce@mit.edu (M.C. Boyce).

0022-5096/$ - see front matter © 2013 Published by Elsevier Ltd.
http://dx.doi.org/10.1016/j.jmps.2012.10.004

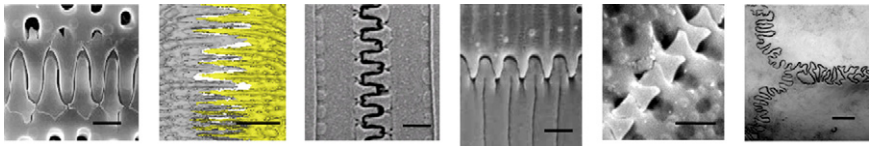

Fig. 1. Various geometries of suture interfaces in biological systems: (a) sinusoidal waveform (scale bar: 1 μm): sutures of diatom *Aulacoseira lirata* (http://westerndiatoms.colorado.edu); (b) triangular waveform(scale bar: 1 mm): stickleback (*Gasterosteus aculeatus*) pelvic suture (Song et al., 2010); (c) trapezoidal waveform (scale bar: 1 μm): suture of diatom (*Ellerbeckia arenaria*) (Gebeshuber et al., 2003); (d) anti-trapezoidal waveform scale bar: 1 μm): suture of diatom (*Aulacoseira ambigua*); (e) complex random waveform (scale bar: 1 cm): cranial suture of white tail deer (*Odocoileus virginianus*).

in nacre-inspired composites (Barthelat et al., 2007; Tang et al., 2007; Espinosa et al., 2011; Barthelat and Zhu., 2011), the intricate geometries of the turtle suture (Krauss et al., 2009), the triangular waveform of the pelvic suture of *Gasterosteus aculeatus* (Li et al., 2011), and the hierarchical fractal-like waveform of the Ammonite septal suture (Li et al., 2012) have each been found to have significant ramifications on mechanical performance. Such structures can often be described as a composite material composed of two stiff interdigitating components (“teeth”) joined by a thinner, relatively compliant interfacial layer along a seam line.

The characterization of the geometry of various natural suture interfaces has been reported (Jaslow, 1990; Long and Long, 1992; Saunders et al., 1999) along with a number of experimental (Hubbard et al., 1971; Jaslow, 1990; Krauss et al., 2009) and numerical studies on these systems (Li et al., 2011; Li et al., 2012; Garcia et al., 2011). For example, cranial bone sutures were found to absorb more energy per unit volume during impact loading than monolithic cranial bone (Jaslow, 1990). In addition, the bending strength of cranial bone sutures was found to increase with an increase in interdigitation (Jaslow, 1990; Jasinoski et al., 2010). A numerical study of a lizard skull with fused and unfused sutures found that suture interfaces can reduce local strain by distributing strain around the skull (Moazen et al., 2009). Studies of ammonites show a trend toward increased septal suture complexity driven by hydrostatic and/or predatory load pressures (Daniel et al., 1997; Saunders et al., 1999; Hassan et al., 2002; De Blasio, 2008). However, a comprehensive and systematically quantitative understanding of the underlying role of geometry on the mechanical behavior and mechanisms is still lacking. Recently, we formulated a scale-independent composite, elastic mechanical model (Li et al., 2011) of a periodic triangular sawtooth suture geometry and showed that suture interfaces with triangular teeth subjected to tension (normal to the suture seam) exhibit a spatially homogeneous stress distribution within both the teeth and interfacial layers, and thus provide an advantage in load transmission, weight, stiffness, strength, energy absorption, and fatigue. We also showed in a second study that increasing the number of hierarchies (hierarchical sutures consist of a superposition of waveforms) in a triangular suture interface resulted in amplification of mechanical properties by orders of magnitude (Li et al., 2012), thus increasing the design parameter space for a given limited material set. These studies addressed a core aspect of the roles of suture geometry in enhancing mechanical performance; however, the scope was limited to a single model system of triangular geometry and the loading case was limited to tension normal to the suture seam.

The goal of the present study is to formulate a generalized suture interface model with arbitrary geometry and, for all in-plane loading cases, to comprehensively explore the role of geometry on the mechanical behavior of suture interfaces. This general theoretical formulation will allow for the interrogation of the functional consequences of the diversity of structural geometries observed in nature and, hence, will provide insights into evolutionary processes. Additionally, guidelines for any specific geometry can be derived to design bio-inspired engineered systems. This paper is organized as follows: in Section 2, the general mechanical model of a suture interface is formulated using the principle of complementary virtual work; in Section 3, the geometric definition of a general trapezoidal suture interface is given; in Section 4, based on the general formulation, the in-plane stiffness tensor, tensile and shear strength and fracture toughness of a periodic general trapezoidal suture interface model are derived and further supported by finite element analysis; in Section 5, using the results in Section 4, the effects of tooth shape on the mechanical properties of the general trapezoidal suture interfaces are compared. Finally, in Section 6, the main conclusions are summarized and potential applications and the relevance to natural systems are discussed.

2. General formulation of the mechanics of the suture interface

2.1. Principle of complementary virtual work

Many biological suture joints and interfaces can be represented as composite materials including at least two phases: a relatively stiff phase ‘1’ and a relatively compliant phase ‘0’, as shown schematically in Fig. 2. The two interdigitating components[1] (phase ‘1’) are joined by a thin, relatively compliant interfacial layer (phase ‘0’) along a suture seam. As the joining zone of two relatively stiff parts located on either a flat or curved surface, the suture interface is often subjected to

[1] In this general formulation, the two interdigitating components are not necessary to be the same material, which means the ‘*i*’ in Eqs. (2) and (3) is not limited to only ‘0’ and ‘1’, for example, the materials can be different (‘phase 1’ and ‘phase 2’) on the two sides of the interfacial layer.

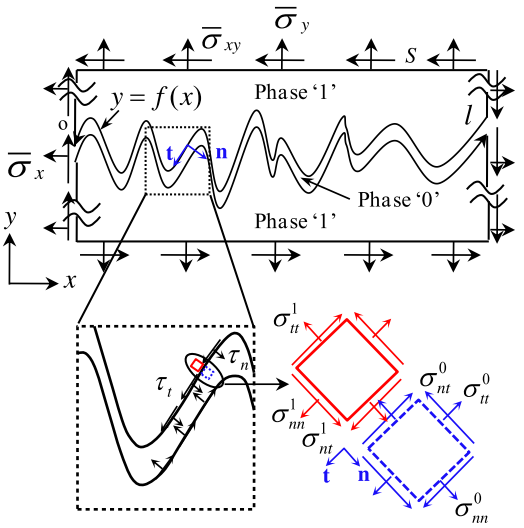

Fig. 2. Schematics of the mechanics of a suture interface with arbitrary geometry showing load transmission and compatibility at the interface.

a far-field traction $\overline{\boldsymbol{\sigma}} = (\overline{\sigma}_x, \overline{\sigma}_y, \overline{\sigma}_{xy})$ along the far-field boundaries S. The profile of the interfacial line l is a function of x in the global coordinate system $x-y$, $y = f(x)$, as shown in Fig. 2.

For a virtual far-field traction $\delta\overline{\boldsymbol{\sigma}} = (\delta\overline{\sigma}_x, \delta\overline{\sigma}_y, \delta\overline{\sigma}_{xy})$, the external complementary virtual work of the system shown in Fig. 2 can be expressed as

$$\delta W_e^* = \int_S \mathbf{u} \cdot \delta\overline{\boldsymbol{\sigma}}\, dS, \tag{1}$$

where $\mathbf{u}$ is the displacement vector at the boundary S. The variation in the complementary strain energy δU^* can be expressed in terms of the strain tensor $\boldsymbol{\varepsilon}$ and the stress tensor $\boldsymbol{\sigma}$ as

$$\delta U^* = \int_V \boldsymbol{\varepsilon} \,:\, \delta\boldsymbol{\sigma}\, dV = \sum_i \int_{V_i} \boldsymbol{\varepsilon}^{\boldsymbol{i}} \,:\, \delta\boldsymbol{\sigma}^{\boldsymbol{i}}\, dV_i\,, \tag{2}$$

where the constitutive equations of each phase, $\boldsymbol{i}$, are

$$\boldsymbol{\sigma}^{\boldsymbol{i}} = \mathfrak{C}^{\boldsymbol{i}} : \boldsymbol{\varepsilon}^{\boldsymbol{i}} \quad (\boldsymbol{i} = 0,1,2\ldots), \tag{3}$$

where, $\mathfrak{C}^{\boldsymbol{i}}$ is the stiffness tensor of phase $\boldsymbol{i}$, which can be either linear or non-linear.

The principle of complementary virtual work yields

$$\int_S \mathbf{u} \cdot \delta\overline{\boldsymbol{\sigma}}\, dS - \int_V \boldsymbol{\varepsilon} : \delta\boldsymbol{\sigma}\, dV = 0. \tag{4}$$

Thus, if we can solve the boundary value problem and find the relationship between the prescribed boundary traction $\delta\overline{\boldsymbol{\sigma}}$ and the virtual responsive stress tensor in each phase $\delta\boldsymbol{\sigma}^{\boldsymbol{i}}$, the closed form solution of the components of the in-plane stiffness tensor can be derived. In order to solve this boundary value problem, a self-contained system of equations is formulated as follows.

2.2. Load transmission

First, loads are transmitted across the interface through normal and/or tangential tractions $\boldsymbol{\tau}(l)$ along the interface (Fig. 2). Force equilibrium gives

$$\begin{cases} \overline{\sigma}_y L_0 = -\int_l \boldsymbol{\tau}(l) \cdot \hat{\mathbf{e}}_{\mathbf{y}}\, dl, \\ \overline{\sigma}_{xy} L_0 = -\int_l \boldsymbol{\tau}(l) \cdot \hat{\mathbf{e}}_{\mathbf{x}}\, dl, \end{cases} \tag{5}$$

where L_0 is the straight end-to-end length of the suture axis, $\hat{\mathbf{e}}_{\mathbf{x}}$ and $\hat{\mathbf{e}}_{\mathbf{y}}$ are the unit vectors in the global coordinate $\mathbf{x}-\mathbf{y}$. The surface traction $\boldsymbol{\tau}(l)$ along the interface can be decomposed in the local coordinate system **t–n** along the interface line l as

$$\boldsymbol{\tau}(l) = \tau_t\, \hat{\mathbf{e}}_{\mathbf{t}} + \tau_n\, \hat{\mathbf{e}}_{\mathbf{n}}, \tag{6}$$

where $\hat{\mathbf{e}}_\mathbf{t}$ and $\hat{\mathbf{e}}_\mathbf{n}$ are the unit vectors in the local coordinate **t–n** and where $\hat{\mathbf{e}}_\mathbf{t}$ is tangent to the suture interface line l and where

$$\begin{cases} \hat{\mathbf{e}}_\mathbf{t}\cdot\hat{\mathbf{e}}_\mathbf{y} = -\hat{\mathbf{e}}_\mathbf{n}\cdot\hat{\mathbf{e}}_\mathbf{x} = -\frac{f'(x)}{\sqrt{1+f'(x)^2}} \\ \hat{\mathbf{e}}_\mathbf{n}\cdot\hat{\mathbf{e}}_\mathbf{y} = \hat{\mathbf{e}}_\mathbf{t}\cdot\hat{\mathbf{e}}_\mathbf{x} = -\sqrt{\frac{1}{1+f'(x)^2}} \end{cases}. \tag{7}$$

Thus, by substituting Eqs. (6) and (7) into Eq. (5), we find

$$\begin{cases} \overline{\sigma}_y = -\frac{1}{L_0}\int_l [\tau_t \hat{\mathbf{e}}_\mathbf{t}\cdot\hat{\mathbf{e}}_\mathbf{y} + \tau_n \hat{\mathbf{e}}_\mathbf{n}\cdot\hat{\mathbf{e}}_\mathbf{y}]\, dl = \frac{1}{L_0}\int_l \left[\tau_t \frac{f'(x)}{\sqrt{1+f'(x)^2}} + \tau_n \sqrt{\frac{1}{1+f'(x)^2}}\right] dl \\ \overline{\sigma}_{xy} = -\frac{1}{L_0}\int_l [\tau_t \hat{\mathbf{e}}_\mathbf{t}\cdot\hat{\mathbf{e}}_\mathbf{x} + \tau_n \hat{\mathbf{e}}_\mathbf{n}\cdot\hat{\mathbf{e}}_\mathbf{x}]\, dl = \frac{1}{L_0}\int_l \left[\tau_t \sqrt{\frac{1}{1+f'(x)^2}} - \tau_n \frac{f'(x)}{\sqrt{1+f'(x)^2}}\right] dl \end{cases}. \tag{8}$$

Eq. (8) shows how the interdigitating interface profile governs the translation of the far-field normal and tangential traction into local normal and tangential traction along the interface. The composition of normal and tangential traction along the interface is determined by the local tangent and the degree of interdigitation of the interface profile.

2.3. Boundary conditions and interface compatibility

At the interface, the two phases satisfy displacement compatibility

$$\mathbf{u}^0(l) = \mathbf{u}^1(l), \tag{9}$$

where $\mathbf{u}^\circ(l)$ and $\mathbf{u}^1(l)$ are displacements along the interface line l.

Also, equilibrium provides the tangential and normal components of the stress tensor, σ^i_{nt} and σ^i_{nn} (i=0 or 1), across the interface to be equal

$$\begin{cases} \sigma^0_{nt} = \sigma^1_{nt} = \tau_t \\ \sigma^0_{nn} = \sigma^1_{nn} = \tau_n \end{cases}. \tag{10}$$

The system of Eqs. (5)–(10) formulates a self-contained boundary value problem for a suture interface with an arbitrary interface profile of finite thickness. For an arbitrary interface profile $y = f(x)$, the mechanical response of the interface can be solved.

One of the main goals of the present study is to explore how to adjust $f(x)$ and $f'(x)$, as shown in Eq. (8), and therefore the coupling between τ_n and τ_t to quantitatively tailor the mechanical performance of an interface layer with a finite thickness. To explain the application of this general formulation, in the next section, we will use Eqs. (1)–(10) to derive a mechanical model of a specific type of interface profile where $f(x)$ is a periodic single (first-order) wave with a general trapezoidal shape.

3. Non-dimensional geometric definition of general trapezoidal suture interfaces

A single-wave triangular suture interface can be described by: the wavelength λ, amplitude A, and the width of interface layer g (Fig. 3). Stiffness and strength can be derived from a scale-independent model (Li et al., 2011) and found to be a function of two independent non-dimensional geometrical parameters, tooth tip angle θ and volume fraction of teeth f_v. These two non-dimensional geometric parameters are related to two other equivalent non-dimensional geometric parameters, the amplitude/wavelength ratio A/λ and the interface width/wavelength ratio g/λ, via

$$\begin{cases} f_v = 1 - \frac{2g}{\lambda} \\ \tan\theta = \frac{f_v \lambda}{2A} \end{cases}. \tag{11}$$

Eq. (11) also holds for all general trapezoidal suture interfaces[2] with the same g, λ, and A.

For a general trapezoidal suture interface (Fig. 3), one additional geometric parameter β is introduced to quantify the shape of the sawteeth; thus β is referred to as the shape factor. Taking y as the direction normal to the suture axis, β is defined as the angle from y to the tooth edge, as shown in Fig. 3a, being positive when the rotation is clockwise and negative when the rotation is counterclockwise. When wavelength λ, amplitude A, and the volume fraction of teeth f_v are fixed, β can only vary in the range of $(-\theta, \theta]$, as shown in Fig. 3a, where θ is a function of λ, A, and f_v, as shown in Eq. (11).

[2] For all general trapezoidal sutures with the same g, λ, and A, the volume/area of the interface in a RVE is $2gA$, and the volume/area of the RVE is λA, thus the volume fraction of teeth in a RVE is $f_v = 1-(2g/\lambda)$. This relation was shown in the literature of triangular suture interfaces (Li et al., 2011, 2012). It holds for all other general trapezoidal shapes as well. As shown in Fig. 3a and c, considering the width g of interface, the width of the root of the triangular teeth is $t = \lambda - 2g = \lambda f_v$, thus $\tan\theta = f_v\lambda/2A$.

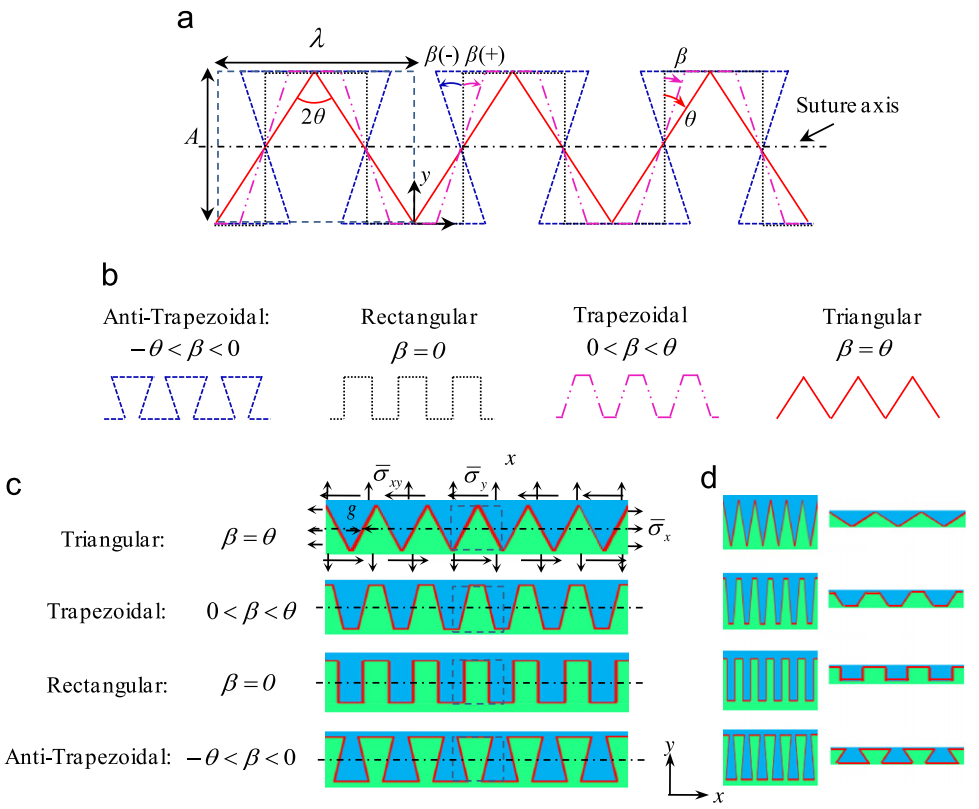

Fig. 3. Schematics of the geometries of general trapezoidal suture interfaces with the same interfacial width g, wavelength λ, and amplitude A: (a) definition of β; (b) representations of four types of general trapezoidal suture interfacial waveform profile; (c) and (d) different geometries for each waveform obtained by varying the wavelength to amplitude ratio λ/A (or θ, when f_v is fixed).

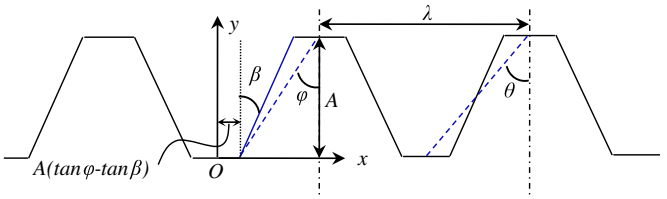

Fig. 4. Geometry of the interface profile of general trapezoidal suture.

The general trapezoidal suture interfaces are categorized into four types according to different ranges of β as shown in Fig. 3b and c: (1) triangular (e.g. Fig. 1b), when $\beta=\theta$, 2θ is the tip angle; (2) trapezoidal (e.g. Fig. 1c), when $0<\beta<\theta$; (3) rectangular, when $\beta=0$; and (4) anti-trapezoidal (e.g. Fig. 1d), when $-\theta<\beta<0$.

Therefore, the geometry of a general trapezoidal suture interface is determined by four independent parameters: the wavelength λ, the amplitude A, the width of the interface g, and the shape factor β. In the local coordinate system (as shown in Fig. 3a) with the origin located at the tip of the triangular wave, the profile of the slant segment of general trapezoidal interface (Fig. 4) is expressed as[3] :

$$w(y)=y\ \tan\beta+A(\tan\varphi-\tan\beta),\quad 0\le y\le A,\quad 0\le w(y)<\frac{\lambda f_v}{2}, \tag{12}$$

where $\tan\phi=(\tan\theta+\tan\beta)/2$. For the entire range of $x\in(-\infty,+\infty)$, waveform functions $w(y)$ of triangular and trapezoidal suture interfaces are single-valued functions, and that of an anti-trapezoidal suture interface is a multi-valued function. The multi-valued anti-trapezoidal shape can provide a mechanical interlocking mechanism even during tension normal to the suture whereas the trapezoidal, rectangular, and triangular only provide interlocking during lateral tension and shear.

[3] $x=w(y)$ is the inverse function of $y=f(x)$.

The scale-independent geometry of the general trapezoidal suture interfaces is determined by three nondimensional parameters: the shape factor β, the volume fraction of teeth f_v (f_v is directly related to the ratio of interface width to wavelength g/λ, as shown in Eq. (11)), and the tip angle of a triangular suture interface 2θ (for an arbitrary shape, θ, describes the ratio of the amplitude to wavelength A/λ when the tooth volume fraction f_v is fixed, as shown in Eq. (11)). Schematics of representative geometries obtained by varying these parameters at fixed f_v are shown in Fig. 3c. Geometries with various f_v can be easily obtained by changing the width of the interface of those shown in Fig. 3c while keeping two other parameters fixed. The geometry-dependent mechanical properties of general trapezoidal suture interfaces, including stiffness, strength and fracture toughness, will be studied in the following sections.

4. Mechanical model of general trapezoidal suture interfaces

4.1. In-plane elastic moduli of general trapezoidal suture interfaces

Suture interfaces act to join two relatively flat or low curvature regions. As a major joining mechanism in the assembly of biological systems, suture interfaces often accommodate local motion such as respiration or growth to enable the daily motion of the whole biological system, and provide support as well as flexibility, distributing load and absorbing energy. Thus, the loads acting on suture interfaces are primarily quasi-static and in-plane for physiological functions in the elastic regime, although sometimes bending or occasional impact loading can be out-of-plane (Jaslow, 1990). In this paper, we address the mechanical behavior within the plane focusing first on the in-plane elastic moduli of suture interfaces. Of particular interest is the effective mechanical properties of the interdigitating area. Therefore, the far-field boundary in the general formulation now becomes the boundary of this area; thus the traction at the boundary is $\overline{\boldsymbol{\sigma}} = (\overline{\sigma}_x,\ \overline{\sigma}_y, \overline{\sigma}_{xy})$ as shown in Fig. 3c.

If two phases, the skeleton and the interface, are assumed in the suture area, Eqs. (2) and (4) yield

$$\int_S \mathbf{u}\cdot\delta\overline{\boldsymbol{\sigma}}\, dS = \int_{V_0} \boldsymbol{\varepsilon}^0 : \delta\boldsymbol{\sigma}^0\, dV_0 + \int_{V_1} \boldsymbol{\varepsilon}^1 : \delta\boldsymbol{\sigma}^1\, dV_1. \tag{13}$$

By alternately prescribing $\overline{\boldsymbol{\sigma}} = (\overline{\sigma}_x, 0, 0)$, $\overline{\boldsymbol{\sigma}} = (0, \overline{\sigma}_y, 0)$, and $\overline{\boldsymbol{\sigma}} = (0, 0, \overline{\sigma}_{xy})$, the corresponding in-plane stiffness components (E_x, E_y, G_{xy}) of the general trapezoidal suture interfaces can be derived, respectively, as shown in the following subsections. The analytical derivations make the following assumptions:

(1) The flat tip region of the suture is taken to be unbonded. (In the current paper, we primarily focus on sutures where the tip region is unbonded and evaluate the contributions of the slant interfacial segment of the general trapezoidal suture interface to stiffness, strength and toughness. The role of the tip region is briefly discussed and left for more detailed examination in a future work. Lin et al. (in preparation).)
(2) The slant interfaces are taken to be perfectly bonded to the teeth.
(3) Both phases are taken to be homogeneous, linear elastic and isotropic.

4.1.1. In-plane tensile (and compressive) moduli

4.1.1.1. Analytical derivation. A virtual longitudinal normal traction (tensile or compressive) $(0, \delta\sigma_y, 0)$ is assumed along the tooth base (loading edge) resulting from far-field loading $\delta\overline{\sigma}_y = \delta\sigma_y(t/\lambda)$ (t is the width of the tooth base, as shown in Fig. 5a)

$$\delta\overline{\sigma}_y = \delta\sigma_y \frac{t}{\lambda} = \delta\sigma_y f_v \left(\frac{\tan\varphi}{\tan\theta}\right). \tag{14}$$

This traction transmits across the interdigitating suture seam, generating a virtual normal traction $\delta\tau_n$ and tangential traction $\delta\tau_t$, along the interface, as shown in Fig. 5a.

Force equilibrium of an isolated tooth (Eqs. (8) and (11)) yields a relation between $\delta\sigma_y$, $\delta\tau_n$ and $\delta\tau_t$

$$\begin{cases} \delta\tau_t = \delta\sigma_y \tan\varphi \cos^2\beta \\ \delta\tau_n = \delta\tau_t \tan\beta = \delta\sigma_y \tan\varphi \sin\beta\cos\beta. \end{cases} \tag{15}$$

Similarly, when the suture interface is subjected to a lateral virtual normal traction $\delta\sigma_x$, the load is transmitted through the virtual interfacial normal traction $\delta\tau_n$ and tangential traction $\delta\tau_t$, as shown in Fig. 5b. Force equilibrium of an isolated tooth yields

$$\begin{cases} \delta\tau_n = \delta\sigma_x \cos^2\beta \\ \delta\tau_t = \delta\tau_n \tan\beta = \delta\sigma_x \sin\beta\cos\beta \end{cases}. \tag{16}$$

If we assume that the teeth are deformable, the total complementary deformation energy δU^* of the suture interfaces is from both the interface and the teeth

$$\delta W_e^* = \frac{A\lambda\overline{\sigma}_y}{E_y}\delta\overline{\sigma}_y = \int_{V_0} \boldsymbol{\varepsilon}^0 : \delta\boldsymbol{\sigma}^0\, dV_0 + \int_{V_1} \boldsymbol{\varepsilon}^1 : \delta\boldsymbol{\sigma}^1\, dV_1 = \delta U^*, \tag{17}$$

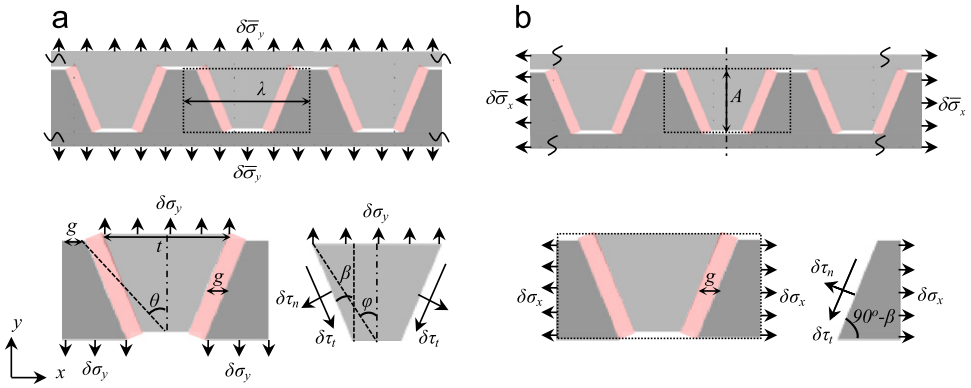

Fig. 5. Free body diagrams of representative volume elements (RVE) of a general trapezoidal suture interface model and its corresponding isolated tooth: (a) under longitudinal tension and (b) under lateral tension ('lighter gray' trapezoid represents the top row of teeth, 'darker gray' trapezoids represents the lower row of teeth, 'pink' rectangles represents the interfacial layer). (For interpretation of the references to color in this figure caption, the reader is referred to the web version of this article.)

where E_y is the effective longitudinal tensile stiffness of the suture interface

$$\delta\sigma^0 = \begin{pmatrix} \delta\tau_n & \delta\tau_t \\ \delta\tau_t & \nu_0\delta\tau_n \end{pmatrix}$$

(in the local coordinate **t–n**) is the position-dependent stress tensor of the interface layer; $\boldsymbol{\sigma}^{\mathbf{1}}$ is the position-dependent stress tensor of the teeth, which we can approximate as

$$\delta\boldsymbol{\sigma}^{\mathbf{1}} = \begin{pmatrix} \delta\sigma_{yy}(y) & 0 \\ 0 & 0 \end{pmatrix}$$

(in the global coordinate x–y), where $\sigma_{yy}(y)$ is derived in the Appendix A; V_0 is the volume of the interface material in the representative volume element (RVE), and $(V_0/V)=1-f_v$, V_1 is the volume of the teeth in an RVE.

If we assume the stress and strain along the interface is uniform, we have

$$\begin{cases} \int_{V_0} \boldsymbol{\varepsilon}^0 : \delta\boldsymbol{\sigma}^0 \, dV_0 = (1-f_v)A\lambda\left[\frac{\tau_n}{E_0^{PS}}\delta\tau_n + \frac{\tau_t}{G_0}\delta\tau_t\right] \\ \int_{V_1} \boldsymbol{\varepsilon}^1 : \delta\boldsymbol{\sigma}^1 \, dV_1 = 4\int_0^A \frac{\sigma_{yy}(y)^2}{E_1} f(y)\delta\sigma_{yy}(y)\, dy \end{cases}, \tag{18}$$

where E_0^{PS} and G_0 are the plane strain modulus[4] and shear modulus of the interfacial material, respectively. By substituting Eqs. (14) and (15) into Eqs. (17) and (18), the effective tensile stiffness of general trapezoidal suture interfaces, E_y, is obtained

$$E_y = f_v\left[\left(\frac{1}{f_v}-1\right)\tan^2\theta\left(\frac{\cos^2\beta\,\sin^2\beta}{E_0^{PS}} + \frac{\cos^4\beta}{G_0}\right) + \frac{\zeta(\beta,\theta)}{E_1}\right]^{-1}, \tag{19a}$$

where

$$\zeta(\beta,\theta) = \begin{cases} 1 & \text{if } \beta=\theta \\ \frac{2}{3}\frac{\tan\theta}{\tan\varphi} & \text{if } \beta=0 \\ 2\frac{\tan\theta}{\tan\varphi}\left[0.5-a+a^2\ln\left(1+\frac{1}{a}\right)\right] & \text{if } \beta\in(-\theta,\ 0)\cup(0,\ \theta) \end{cases}, \tag{19b}$$

and where

$$a = \frac{\tan\varphi}{\tan\beta} - 1. \tag{19c}$$

If we assume the teeth are rigid and the strain energy only comes from the deformation of the interface layer, the stiffness of the rigid tooth model can be obtained simply by taking $\zeta(\beta,\theta)=0$ in Eq. (19a). When $\beta=\theta$, Eq. (19b) reduces to the longitudinal tensile stiffness of a triangular suture interface (Li et al., 2011).

[4] $E_0^{PS} = (E_0/1-\nu_0^2)$, E_0 and ν_0 are Young's modulus and Poisson's ratio of the interface material.

Similarly, the lateral tensile stiffness of a general trapezoidal suture interface, E_x is obtained as

$$E_x = \left[(1-f_v)\left(\frac{\cos^2\beta\sin^2\beta}{G_0}+\frac{\cos^4\beta}{E_0^{PS}}\right)+\frac{f_v}{E_1}\right]^{-1}. \tag{20a}$$

If we assume the teeth are rigid, the stiffness becomes

$$E_x^{RTM} = \left[(1-f_v)\left(\frac{\cos^2\beta\sin^2\beta}{G_0}+\frac{\cos^4\beta}{E_0^{PS}}\right)\right]^{-1}. \tag{20b}$$

From Eqs. (19) and (20), it can be seen that both E_y and E_x depend on the material properties of the two phases,E_0^{PS}, G_0, E_1, and the volume fraction of teeth f_v. However, E_y depends on geometry through both β and θ and on geometry only through β. Results will be shown together with supporting finite element simulations below.

4.1.1.2. Finite element simulations. Finite element simulations of four types of general trapezoidal suture interfaces (with $\theta=21.8^\circ$, and $\beta=21.8^\circ$, 11.3°, 0° and -11.3°, respectively) under longitudinal, lateral tension and shear are processed. Representative volume elements are identified and subjected to periodic boundary conditions consistent with the three loading conditions. The periodic boundary conditions follow the general approach in Danielsson et al. (2002) and the loading conditions can be found in Appendix B.

4.1.1.3. Case of bonded flat tip regions. We first briefly present results considering the tip region to be perfectly bonded prior to the more detailed comparisons of cases with unbonded tips. In Fig. 6a, finite element simulation results for cases considering the tip region to be perfectly bonded clearly show that the stress in the triangular teeth (i.e. when $\beta=\theta$) is very close to uniform (with an exception of a singularity at the very tip) and show the other three geometries (when $\beta\neq\theta$) to have stress gradients with concentrations at the base of the teeth, as expected. The degree of stress concentration increases when β decreases, with the anti-trapezoidal shape having the strongest stress concentration.

Also, as expected and shown in Fig. 6b, the interface strain is highest in the interface regions across the flat tip, and the tooth stress (Fig. 6a) is highest in the tooth base away from the flat tip, indicating that the first failure events will occur at these flat tips (for triangular suture interface, the flat tip degenerates into a singular point). For completeness, Appendix C compares the initial stiffness of general trapezoidal suture interfaces with bonded and those with unbonded flat tip interfaces. As expected, the flat tip interface increases the initial effective stiffness of the suture interface (Table C1), but would fail first due to the large strain concentration (Lin et al., in preparation). However, we note that the failure of the tip material does not result in fatal failure of the suture interface. After flat tip interface failure, load is transmitted only through the shear and normal stress along the angled interface. These slant interfaces then control the stiffness, the strength and the toughness of the suture. In this paper, we focus on evaluating the role of the slant segments of the interfaces and will report on the role of flat tips via simulations and experiments in Lin et al. (in preparation). Hence, the analytical expressions given in Eqs. (19) and (20) coincide with finite element simulations conducted on the different geometries with unbonded flat tips.

4.1.1.4. Cases of unbonded tip regions. Two-dimensional plane stress finite element simulations of longitudinal and lateral tension were conducted for the four types of suture interfaces with unbonded tip regions taking the case of wavelength $\lambda=1.25$ mm, amplitude $A=1.25$ mm, and a volume fraction of teeth $f_v=80\%$. This geometry gives $\theta=21.8^\circ$, and for the

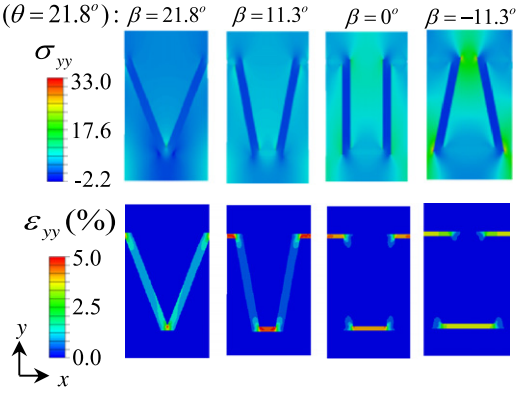

Fig. 6. Stress/strain contours of trapezoidal suture interfaces of varying geometry subjected to longitudinal tension from finite element simulations ($E_1=10$ GPa, $E_0=100$ MPa, $f_v=0.8$), (a) longitudinal stress contour and (unit: MPa) (b) strain contour.

anti-trapezoidal, rectangular, trapezoidal and triangular geometries, the shape factors β are -11.3°, 0°, 11.3°, and 21.8°, respectively. The stiffness ratio R_s between two phases is defined as $R_s = E_1/E_0$, and is varied from 10 to 1000 in the FE simulations. The in-plane moduli are obtained from these FE simulations for comparison to the analytical results (Eqs. (19) and (20)) in Fig. 7.

For longitudinal and lateral tension, Fig. 7 shows that the stresses in the teeth are uniform when $\beta = \theta$; in contrast, when $\beta \neq \theta$, the stresses are not uniform (see Appendix A for the derivation of the stress distribution). For both cases, the analytical results for trapezoidal suture interfaces are quite accurate in predicting the longitudinal and lateral stiffness for all values of β. The triangular suture exhibits a longitudinal tensile stiffness that is maximum among the four types, while its lateral stiffness is the minimum. However, it is opposite for rectangular suture interfaces. For rectangular suture interfaces with rigid teeth, the interface is under pure shear in longitudinal tension and thus is the most compliant, while it is under pure tension in lateral tension and thus is the stiffest. For all other shapes the interface is under a combined shear and tension, as shown in Eq. (15).

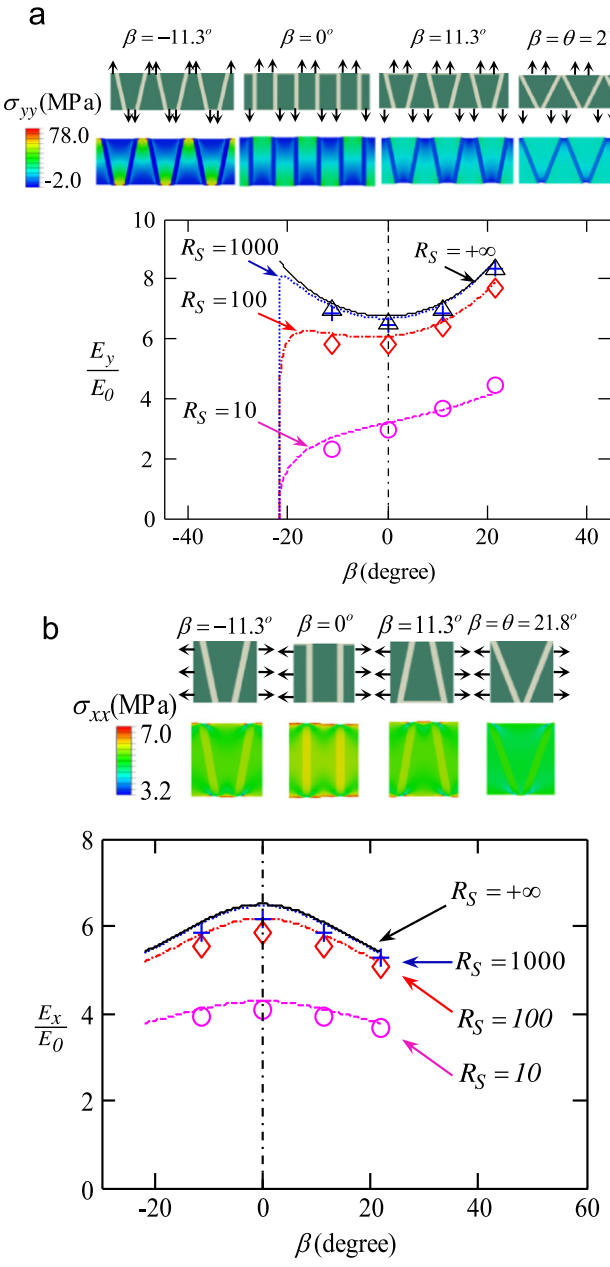

Fig. 7. Comparison of finite element results (symbols) and analytical (lines) results of longitudinal and lateral tensile stiffness of general trapezoidal suture interfaces, changing with β ($-\theta < \beta < \theta$, $\theta = 21.8^\circ$, i.e. $A/\lambda = 1$, and $f_v = 0.8$), under (a) longitudinal tension, and (b) lateral tension.

As can be seen in Eqs. (19), when the teeth are rigid ($R_S \to +\infty$), the longitudinal stiffnesses are symmetric about $\beta=0$ because, physically, the stiffness of the rigid tooth model is governed by deformation of the interface and the stress distribution in the interfaces is symmetric about $\beta=0$. However, as shown in Fig. 7a, when the teeth are deformable, the longitudinal stiffness is not symmetric about $\beta=0$, because the stress distributions within the trapezoidal versus the anti-trapezoidal teeth are different and hence their contributions to the overall stiffness differ (shown in Fig. 7a and the Appendix A). This is most clear by noting the reduced net cross-sectional area of the anti-trapezoidal versus trapezoidal tooth root which results in very different strain energy stored in the teeth for the two cases of β and $-\beta$. Furthermore, when $\beta=-\theta$, the cross-sectional area of the tooth root decreases to zero and hence the tensile stiffness is zero for all finite stiffness ratios, as shown in Fig. 7a.

As can be seen in Eqs. (20) and Fig. 7b, the lateral stiffness is always symmetric about $\beta=0$, whether the teeth are rigid or deformable. This is because, physically, for the cases of shape factors β and $-\beta$, the stress states in the interface layers and in the teeth are the same, as shown in Eqs. (20) and the stress contours shown in Fig. 7b.

4.1.2. In-plane shear

4.1.2.1. Analytical derivation. A virtual tangential traction $\delta\sigma_{xy}$ along the tooth base resulting from far-field tangential traction $\delta\overline{\sigma}_{xy}$ transmits across the interdigitating suture seam and generates a responsive tangential traction $\delta\tau_t$, and normal traction $\delta\tau_n$ along the interface, as shown in Fig. 8a.

The effective far-field virtual tangential traction $\delta\overline{\sigma}_{xy}$ is related to the virtual tangential traction $\delta\sigma_{xy}$ at the base of the teeth via simple weighting of the load bearing areas (refer Figs. 3c and 8a)

$$\delta\overline{\sigma}_{xy}=\frac{t}{\lambda}\delta\sigma_{xy}=f_v\left(\frac{\tan\varphi}{\tan\theta}\right)\delta\sigma_{xy}. \tag{21}$$

The force equilibrium of an isolated tooth (Eqs. (8) and (11)) yields the relation between $\delta\sigma_{xy}$ and $\delta\tau_n$ and $\delta\tau_t$ as

$$\delta\sigma_{xy}=\frac{\delta\tau_t\tan\beta+\delta\tau_n}{\tan\varphi}. \tag{22}$$

Similar to the derivation of tensile stiffness, the shear modulus of a general trapezoidal suture is derived as (a detailed derivation is given in Appendix D)

$$G_{xy}(\theta,\beta)=\frac{f_v^2E_0E_1C'(\beta)}{f_vE_0C'(\beta)C^b+E_1(1-f_v)\tan^2\theta+E_1\tan\theta\tan\beta C^r}, \tag{23a}$$

where C^b and C^r are functions of θ

$C^b=\frac{3E_1}{4G_s}+\frac{5}{16}(\tan\theta)^{-2}$, $C^r=\frac{3G_0}{2G_s}+\frac{9}{8}\frac{G_0}{E_1}(\tan\theta)^{-2}$,which are consistent with Li et al. (2012); also, C^b is related to bending-induced deflection Δ_b via $C^b=f_v(\Delta_b/A)(E_1/\overline{\sigma}_{xy})$, C^r is related to shear-induced angle change γ_b via $C^r=f_v\gamma_b(G_0/\overline{\sigma}_{xy})$; and $C'(\beta)=(G_0/E_0)(\tan\beta)^2+\left(E_0^{PS}/E_0\right)$.. When $\beta=\theta$, Eq. (23a) reduces to the shear stiffness for a triangular suture interface, as derived by Li et al. (2012). When the teeth are rigid, $C^b=0$ and $C^r=0$, so the shear modulus is simply

$$G_{xy}^{RTM}=\frac{f_v^2E_0C'(\beta)}{(1-f_v)\tan^2\theta}=\frac{f_v^2}{(1-f_v)}\frac{1}{\tan^2\theta}\left(E_0^{PS}+G_0\tan^2\beta\right). \tag{23b}$$

4.1.2.2. Finite element simulations. The deformation mechanisms (including both bending and shear) of the teeth under effective simple shear (Fig. 8b, right) at the boundary are visualized through finite element simulations of triangular suture interfaces with various θ. Fig. 9 depicts the deformation of teeth for sutures with different stiffness ratios. The combined shear and bending of the teeth are clearly shown, with bending becoming more dominant as stiffness ratio increases (Li et al., 2012). The local normal stress σ_{yy} in the teeth reaches a maximum value at the corners of the tooth base for all

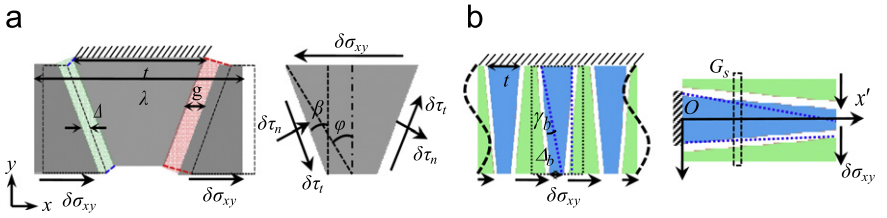

Fig. 8. Schematics of force equilibrium of a general trapezoidal suture interface model and the free body diagram of an isolated tooth under shear loading, (a) when teeth are rigid, and (b) when teeth are deformable (coupling shear and bending effects, 'blue' represents the top row of teeth, 'green' represents the lower row of teeth, 'pink' represents the interfacial layer). (For interpretation of the references to color in this figure caption, the reader is referred to the web version of this article.)

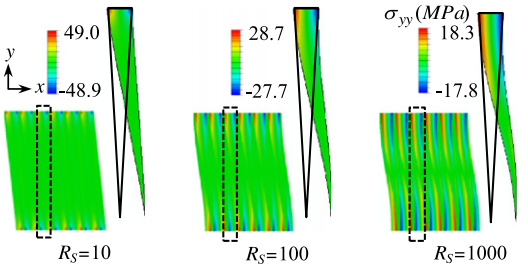

Fig. 9. Deformation of a tooth in triangular suture interfaces subject to simple shear for stiffness ratios of 10, 100 and 1000, and for $\theta = 2.9^\circ$ and $f_v = 0.8$ (the contour shown is at 1% overall shear strain, the deformation is amplified by a factor of 10).

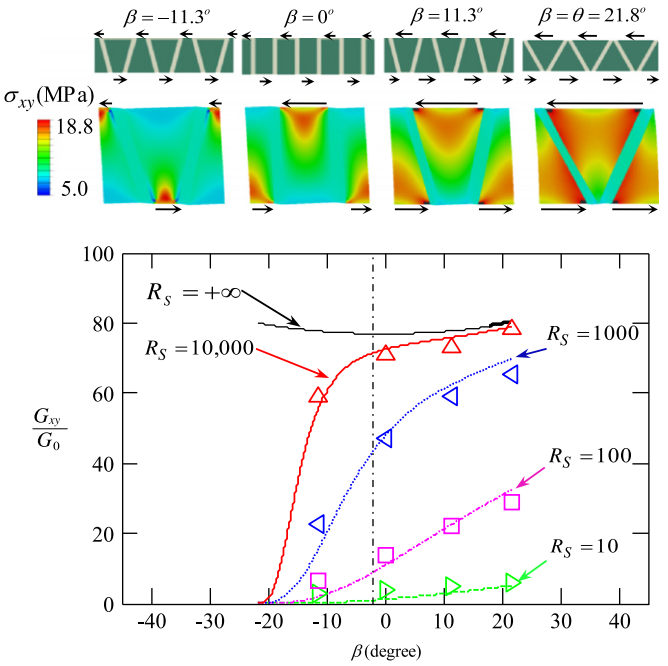

Fig. 10. Comparison of finite element (symbols) and analytical (lines) results of effective shear moduli as a function of shape factor β, i.e. for four types of general trapezoidal suture interfaces.

stiffness ratios as a result of the bending moment being greatest at this location, as shown in Fig. 9.

Finite element simulations of the four types of general trapezoidal geometries under simple shear are processed for the case of $\theta = 21.8^\circ$, $f_v = 0.8$ and for $\beta = -11.3^\circ$, 0°, 11.3°, and 21.8°, respectively. The finite element results and the analytical results of the shear moduli for different β and R_S are compared in Fig. 10.

It can be seen in Fig. 10 that when the teeth are rigid ($R_S \to +\infty$), the shear modulus is symmetric about $\beta = 0^\circ$. The rectangular suture geometry gives the smallest shear stiffness because the interfaces are only under pure tension and compression, while the interfaces for other shapes are under the same tension and compression as well as a component of shear, and therefore the higher strain energy of deformation makes these interfaces stiffer.

When the teeth are deformable, the shear modulus monotonically increases with β, as can be seen in Fig. 10. At a certain effective shear strain (Δ/A), when β increases, the strain energy in the teeth and the total strain energy of the suture interface increase. When β is negative, the shear modulus is very sensitive to β, especially for high stiffness ratios. This is because when β is close to $-\theta$, either the effective bending or shear resistance of the teeth approaches zero (since the tooth end has the smallest net section and hence the least stiffness to bending and shear). On the other hand, when β is positive, the shear modulus is much less sensitive to β.

4.1.3. *Parametric study of the influence of tooth angle on stiffness components for various geometries and material compositions*

Analytical expressions (Eqs. (19), (20)–(23)) of the in-plane components of the normal and shear stiffness components E_y, E_x and G_{xy} were found as a function of material properties E_0^{PS}, G_0, E_1, G_1 and geometric parameters β, f_v and θ. In this section, the dependence of the non-dimensional effective stiffness components E_y/E_0, E_x/E_0, and G_{xy}/G_0 on geometry and stiffness ratio are examined. E_y/E_0, E_x/E_0, and G_{xy}/G_0 are plotted in Fig. 11 as a function of tooth angle θ by using Eqs. (19)–(23).

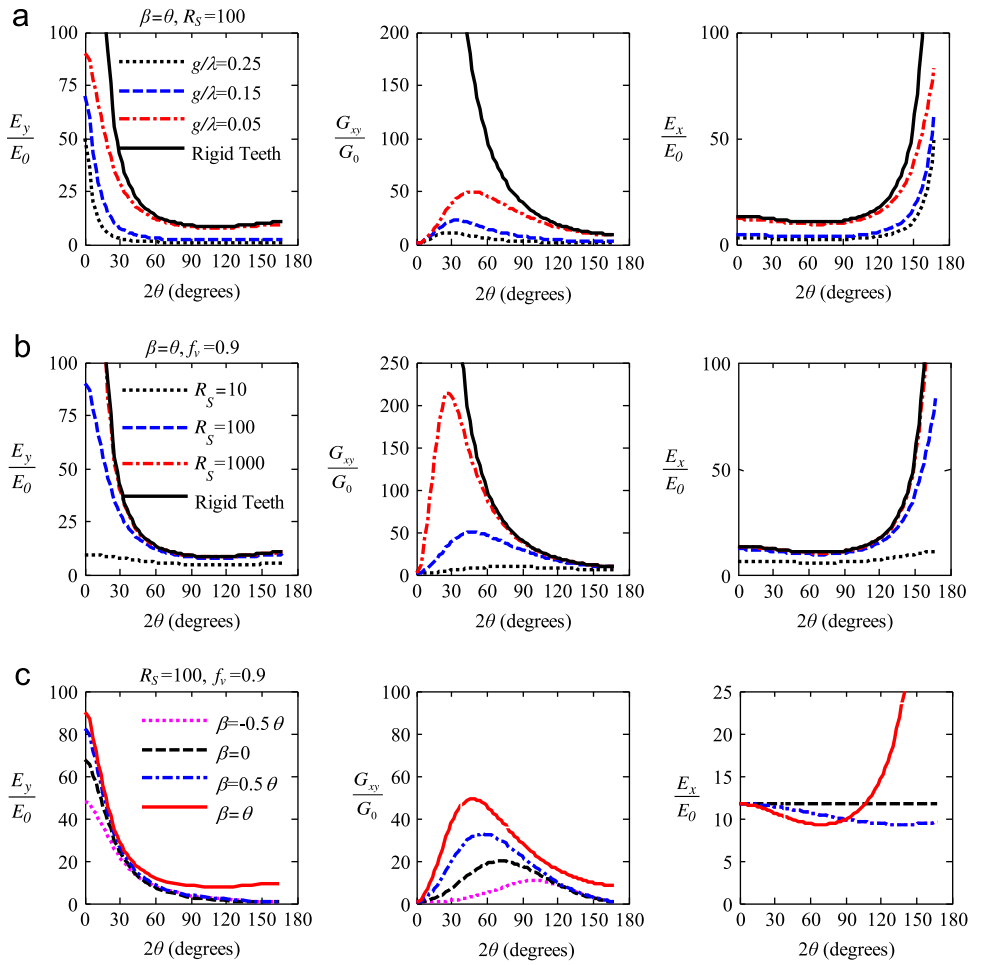

Fig. 11. Analytical results of the in-plane moduli and their relations to geometric and material parameters of single-waved suture interfaces, (a) influences of the non-dimensional interface width, (b) influences of stiffness ratio, and (c) influence of θ and β on the amplification of in-plane moduli.

Fig. 11 shows that each of the three stiffness components is highly nonlinearly related to tooth tip angle. Generally, for all types of general trapezoidal suture interfaces, the longitudinal stiffness E_y/E_0 increases when the tip angle decreases, as shown in Fig. 11 (left column). For very small tip angles, E_y/E_0 increases very rapidly towards Voigt law when θ approaches zero. For relatively large θ, the E_y/E_0 predicted by the rigid tooth model and the deformable tooth model are close, as shown in Fig. 11a and b, since the applied deformation is primarily accommodated by the interface. However, when θ is small, the rigid tooth model overestimates the stiffness and the deformation of teeth must be considered. The trends of lateral stiffness E_x/E_0 for relatively large and small tip angles are opposite to those of the longitudinal stiffness, as expected, with E_x/E_0 increasing rapidly when θ increases towards π, as shown in Fig. 11 (right column). The lateral stiffness of rectangular suture interfaces does not depend on θ (where 2 tan θ is the aspect ratio for rectangular teeth), and the lateral stiffnesses of trapezoidal and anti-trapezoidal suture interfaces are the same.

The shear stiffness G_{xy}/G_0 increases with decreasing θ for the rigid tooth model (RTM) since shear deformation must be fully accommodated by the interface layer. However, for the DTM, the suture shear stiffness exhibits a peak at a θ that depends on the stiffness ratio due to the relative contributions of shear and bending of the teeth to the overall deformation. When the tip angle is either very small or very large, G_{xy}/G_0 is very small, as shown in the middle figures of Fig. 11 (center column). When R_S or β increases, the peak of shear modulus shifts to the left (i.e. shift to smaller tip angles); while when g/λ decreases, the peak of shear modulus shifts to right (i.e. shifts to larger tip angles). Also, it can be seen from Fig. 11 that when the interface width to wavelength ratio g/λ decreases (i.e. the volume fraction increases), or when the stiffness ratio R_S increases, or when β increases, all three stiffness components increase.

4.1.4. *Anisotropy ratio*

As one measure of anisotropy, we take the anisotropy ratio E_y/E_x. Here, E_y/E_x for the triangular suture interfaces is plotted as a function of θ for various R_S, f_v and β as shown in Fig. 12a, b and c, respectively. As expected, the anisotropy ratio is close to one in the middle range of θ (θ near 45°) for all values of R_S, f_v and β since the interface will have the same

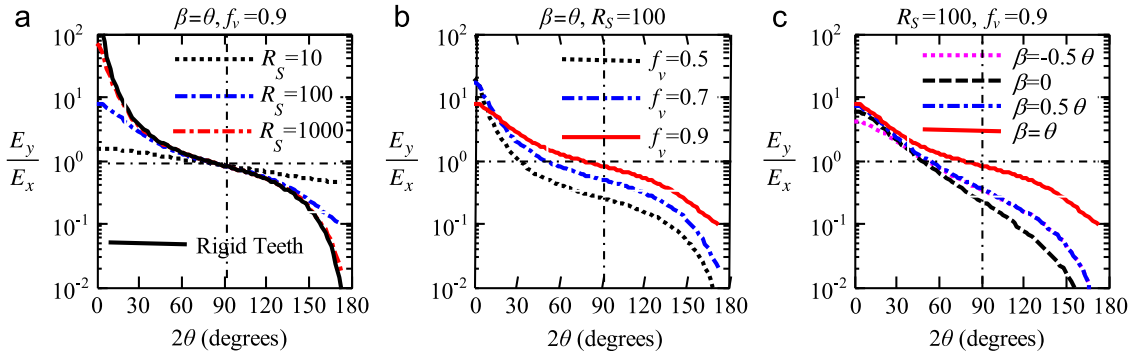

Fig. 12. Anisotropy ratio E_y/E_x vs. θ for various tooth/interface stiffness ratio (a), volume fraction of teeth (b), and different types of general trapezoidal suture interfaces.

relative local shear and normal stress for both longitudinal and lateral loading when $\theta = 45^\circ$. However, the anisotropy ratios are large for very small or very large tip angles because, as can be seen from Eqs. (19) and (20), the difference between E_y and E_x is positively related to the difference between $\sin^2\beta$ and $\cos^2\beta$, and roughly speaking, $E_y(\theta) \approx E_x(90^\circ - \theta)$. Fig. 12a shows that for either very small or very large θ, the degree of anisotropy increases rapidly when the stiffness ratio increases; while when θ is around 90°, the stiffness ratio has little influence on the anisotropy of suture interfaces due to the more dominant role of interface deformation to overall deformation.

4.2. Strength and failure mechanisms

In this section, failure mechanisms, strength and fracture toughness of general trapezoidal suture interfaces are studied for an idealized scenario of perfect bonding between the two phases, assuming a critical principal stress failure criterion for each phase. Thus, two failure mechanisms are taken to be possible: tooth breakage and interface failure, each taken to occur when the maximum principal stress reaches a critical value. The geometry dependence of the effective tensile and shear strength, toughness, and failure mechanisms of suture interfaces are now explored.

4.2.1. Tension

The failure criterion for a suture interface is taken to be when the maximum principal stress in either teeth or interface layer achieves a critical stress, the tensile strength, of the respective phase material. When the suture interface is under tension, the maximum principal stress σ_0^P in the interface layer is approximated as

$$\sigma_0^P = \frac{(1+\nu_0)\tau_n}{2} + \sqrt{\left[\frac{(1-\nu_0)\tau_n}{2}\right]^2 + (\tau_t)^2}.$$

By using Eq. (15), σ_0^P is expressed as

$$\sigma_0^P = \sigma\, B(\varphi, \beta), \tag{24a}$$

where

$$B(\varphi, \beta) = \frac{\tan\varphi\cos\beta}{2}\left[(1+\nu_0)\sin\beta + \sqrt{(1-\nu_0)^2\sin^2\beta + 4\cos^2\beta}\right], \tag{24b}$$

and where σ is the maximum principal stress in the teeth.

The failure mechanism that will occur is determined by whether σ_0^P reaches the tensile strength σ_0^f of the interfacial material first or if σ reaches the tensile strength σ_1^f of the tooth material first. Therefore, the effective strength $\overline{\sigma}^f$ of the suture interface can be expressed as

$$\overline{\sigma}^f = f_v \sigma_1^f \min\left[\overline{\sigma}_I, \overline{\sigma}_{II}\right], \tag{25a}$$

where $\overline{\sigma}_I$ is the effective suture strength considering tooth failure, and $\overline{\sigma}_{II}$ is the effective suture strength considering interface failure. $\overline{\sigma}_I$ and $\overline{\sigma}_{II}$ are derived as functions of the strength ratio $\left(\sigma_1^f/\sigma_0^f\right)$, θ and β

$$\begin{cases} \overline{\sigma}_I = \frac{\tan\varphi}{\tan\theta} & \left(\text{tooth failure} : \sigma = \sigma_1^f\right) \\ \overline{\sigma}_{II} = \frac{\sigma_0^f}{\sigma_1^f}\frac{\tan\varphi}{\tan\theta B(\varphi,\ \beta)} & \left(\text{interface failure} : \sigma_0^P = \sigma_0^f\right) \end{cases}. \tag{25b}$$

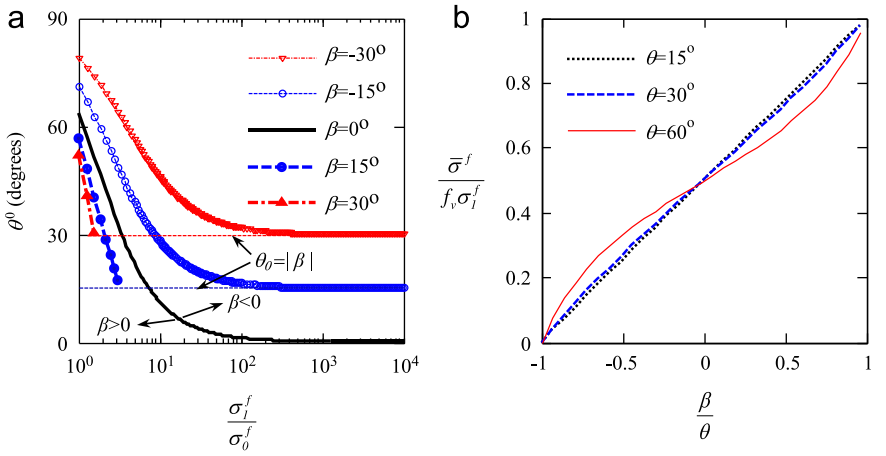

Fig. 13. (a) Optimal θ° in maximizing the effective strength of general trapezoidal suture interfaces vs. strength ratio of the two phases for various β ($\theta^\circ \geq \beta$), (b) non-dimensional strength vs. nondimensional slantness β/θ.

When $\overline{\sigma}_I = \overline{\sigma}_{II}$, the teeth and interface fail simultaneously. Hence, we can derive the tip angle θ° corresponding to the failure mechanism transition as a function of the strength ratio (σ_1^f/σ_0^f) and β

$$\theta^o = \tan^{-1}\left\{\frac{4\sigma_0^f}{\sigma_1^f}\,\frac{1}{\cos\beta\,[(1+\nu_0)\sin\beta+\sqrt{(1-\nu_0)^2\sin^2\beta+4\cos^2\beta}]}-\tan\beta\right\}. \tag{25c}$$

When $\beta=0$, $\theta^o=\tan^{-1}\left(2\sigma_0^f/\sigma_1^f\right)$, which is consistent with the tip angle for failure mechanism transition of rectangular suture interfaces derived using the maximum shear strength criteria for the interfacial material by Li et al. (2011). This is because in this case, the interface is only under shear, hence, the shear stress of the interface equals to the maximum principal stress. When $\theta<\theta^\circ$, tooth failure occurs; when $\theta>\theta^\circ$, the interface fails; and when $\theta=\theta^\circ$, the teeth and interface fail simultaneously.

Eq. (25c) is plotted in Fig. 13(a). It can be seen that for all β values, i.e. for all wave forms, θ° decreases when (σ_1^f/σ_0^f) increases. When $\beta>0$, there is a maximum strength ratio, beyond which θ° does not exist, which means the suture interfaces only fail by interface failure; when $\beta<0$, θ° exists for all values of (σ_1^f/σ_0^f), however, θ° is asymptotic to $|\beta|$ when (σ_1^f/σ_0^f) increases. According to Eqs. (25a) and (25b), the nondimensional effective strength of the suture interfaces $\left(\overline{\sigma}^f/f_v\sigma_1^f\right)$ is plotted as a function of θ, and the nondimensional slantness of the slant interfaces (defined as β/θ), as shown in Fig. 13b. It can be seen that $\left(\overline{\sigma}^f/f_v\sigma_1^f\right)$ increases monotonically with β/θ.

Eqs. (25) show that under tension, when tooth failure occurs, the effective strength is only determined by the geometry and the strength of teeth, independent of strength of the interface; while when interface failure occurs, the effective strength depends on geometry and the strength ratio of the tooth material and interface material (σ_1^f/σ_0^f). By decreasing the strength ratio (σ_1^f/σ_0^f) (i.e. by increasing the interface strength/tooth strength ratio), the effective strength of suture interfaces which exhibit interface failure can be improved significantly.

4.2.2. Shear

Similarly, when the suture interface is subjected to simple shear, the maximum principal stress in the interface layer is approximated as

$$\sigma_{0S}^P = \tfrac{(1+\nu_0)\tau_n}{2}+\sqrt{\left[\tfrac{(1-\nu_0)\tau_n}{2}\right]^2+(\tau_t)^2}.$$

By using Eqs. (21)–(23), τ_t and τ_n are related to the effective far-field shear stress $\overline{\tau}$ via

$$\begin{cases}\tau_t = \frac{\overline{\sigma}_{xy}D_1}{f_v}\\ \tau_n = \frac{\overline{\sigma}_{xy}D_2}{f_v}\end{cases}, \tag{26}$$

where

$$D_1 = \frac{G_0\ \tan\beta}{\tan\theta}\left[\frac{f_v^2}{(1-f_v)G_{xy}}-\frac{f_v}{1-f_v}\frac{C^b}{E_1}\right]-C^r$$
$$= \frac{G_0\ \tan\beta\ \tan\theta+G_0\tan^2\beta\,C^r-E_0C'\,C^r}{E_0C'}$$

and

$$D_2 = \frac{E_0^{PS}}{\tan\theta}\left[\frac{f_v^2}{(1-f_v)G_{xy}} - \frac{f_v}{1-f_v}\frac{C^b}{E_1}\right] = \frac{E_0^{PS}\tan\theta + E_0^{PS}\tan\beta C^r}{E_0 C'}.$$

When the suture interface is subjected to simple shear, the stress distribution in the teeth is no longer uniform and the maximum principal stress σ_{1S}^P is located at the corner of the tooth base, as shown in Fig. 14.

The stress tensor has two main components: the shear component τ and a normal component σ_b due to bending. Therefore, σ_{1S}^P is expressed as

$$\sigma_{1S}^P = \frac{\sigma_b}{2} + \sqrt{\left(\frac{\sigma_b}{2}\right)^2 + \tau^2}.$$

By employing the theory of beam bending, σ_b is related to $\overline{\sigma}_{xy}$ by

$$\sigma_b = \frac{\overline{\sigma}_{xy} D_3}{f_v}, \tag{27}$$

where

$$D_3 = \frac{f_v 6\lambda A}{t^2} = \frac{12\tan\theta}{(\tan\theta+\tan\beta)^2}.$$

Consequently, the effective shear strength of suture interfaces is derived as functions of $\left(\sigma_1^f/\sigma_0^f\right)$, θ and β :

$$\overline{\tau}^f = f_v \sigma_1^f \ \min\left[\overline{\tau}_I,\ \overline{\tau}_{II}\right]. \tag{28a}$$

where the effective strength corresponding to the two failure mechanisms, $\overline{\tau}_I$ and $\overline{\tau}_{II}$ are

$$\begin{cases} \overline{\tau}_I = \left\{\frac{D_3}{2} + \sqrt{\left(\frac{D_3}{2}\right)^2 + \left(\frac{\tan\varphi}{\tan\theta}\right)^{-2}}\right\}^{-1} & \left(\text{tooth failure} : \sigma_{1S}^P = \sigma_1^f\right) \\ \overline{\tau}_{II} = \frac{\sigma_0^f}{\sigma_1^f}\left\{\frac{(1+v_0)D_2}{2} + \sqrt{\left[\frac{(1-v_0)D_2}{2}\right]^2 + [D_1]^2}\right\}^{-1} & \left(\text{interface failure} : \sigma_{0S}^P = \sigma_0^f\right) \end{cases}. \tag{28b}$$

Similar to the case of tension, when $\overline{\tau}_I = \overline{\tau}_{II}$, the teeth and interface fail simultaneously. Hence, the tip angle θ_S^o corresponding to the failure mechanism transition can be determined. The θ_S^o for shear failure mechanism transition is not only determined by the strength ratio and geometry $\left(\left(\sigma_1^f/\sigma_0^f\right),\ \theta \text{ and } \beta\right)$, but also determined by the stiffness ratio of the two phases, because D_1 and D_2 are functions of stiffness ratio. However, the θ° for tensile failure mechanism transition does not depend on the stiffness ratio.

Eqs. (28) show that under simple shear, when tooth failure occurs, the effective strength is only determined by the geometry and the strength of teeth, independent of the strength of the interface; while when interface failure occurs, the effective strength depends on geometry and the strength ratio of the interface material and tooth material. By decreasing the strength ratio, the effective strength of suture interfaces which exhibit interface failure can be improved significantly. However, interface failure will not lead to the catastrophic failure of the suture interface due to the interlocking of teeth during shear, which means the suture interfaces still can take shearing load even after the interface fails.

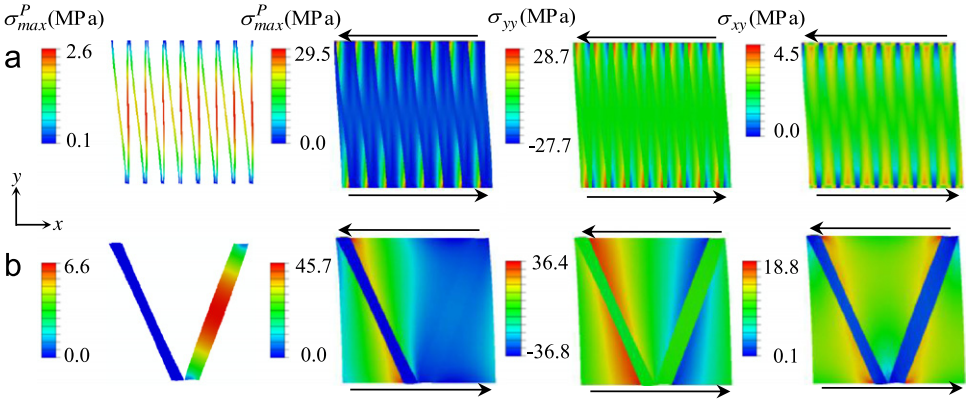

Fig. 14. Distribution of maximum principal stress σ_{max}^P, stress component due to bendingσ_{yy} and that due to shear σ_{xy}, for a case of (a) small tip angle, θ=2.9°, and (b) a case of relatively large tip angle, θ=21.8°.

4.3. Fracture toughness

The non-dimensional tensile fracture toughness $\overline{\Gamma}^f$ and shear fracture toughness $\overline{\Gamma}_S^f$ of a suture interface are defined as

$$\begin{cases} \overline{\Gamma}^f = \left(\dfrac{\overline{\sigma}^f}{\sigma_1^f}\right)^2 \dfrac{E_1}{E_y} \\ \overline{\Gamma}_S^f = \left(\dfrac{\overline{\tau}^f}{\sigma_1^f}\right)^2 \dfrac{G_1}{G_{xy}} \end{cases}, \tag{29}$$

where expressions for $\overline{\sigma}^f$ and $\overline{\tau}^f$ were given in Eqs. (25) and (28), respectively. $\overline{\Gamma}^f$ and $\overline{\Gamma}_S^f$ are highly nonlinear functions of θ and f_v, monotonically decreasing with an increase in f_v and exhibiting a non-monotonic dependence on θ. The non-dimensional tensile fracture toughness is expected to reach an optimum at θ° (shown in Eq. (25c)) dependent on β and the strength ratio, which corresponds to a simultaneous failure of the interface and teeth, i.e. at the point of failure mechanism transition, because the strength of both materials are fully utilized.

Quantitative plots of the analytical solutions derived in this section will be presented in the next section.

5. Effect of tooth shape on stiffness, strength, and toughness

Based on the analytical derivations in Section 4, comparisons of both tensile and shear stiffness, strength, failure mechanisms and fracture toughness for four general trapezoidal suture interfaces of different θ are now presented. The four types of general trapezoidal suture interfaces are represented by taking $\beta = \theta$ (triangular), $\beta = 0.5\theta$ (trapezoidal), $\beta = 0$ (rectangular), and $\beta = -0.5\theta$ (anti-trapezoidal), respectively.

5.1. Tension

Schematics of the two failure mechanisms of the four types of general trapezoidal suture interfaces under tension are shown in Fig. 15a. Stiffness, strength and fracture toughness of these four types of suture interfaces are plotted and compared in Fig. 15b, c and d, respectively.

Fig. 15b–d shows that the tensile stiffness, strength and fracture toughness of all the general trapezoidal wave-forms are significantly improved with a flat interface, especially for relatively small θ. When θ is small, the stiffness, strength and fracture toughness are strongly dependent on β. However, when θ increases, these differences diminish and the stiffness, strength and fracture toughness asymptote to those of flat interfaces.

When θ is small, Fig. 15b, c and d shows that the stiffness, maximum strength and maximum toughness of the four types of general trapezoidal suture interfaces follow a ranking of triangular > trapezoidal > rectangular > anti-trapezoidal. The reduced net load-bearing section of the tooth base leads to higher stress in the anti-trapezoidal teeth and hence reduced strength; the differences in the stress distribution also correspond to the reduced energy stored in the anti-trapezoidal teeth and hence stiffness decreases. Interestingly, as shown in Fig. 15d, a cusp forms at the point of failure mechanism transition and the peak tensile fracture toughness is achieved when the failure mechanism transition occurs. The fracture toughness reduces rapidly on both sides of the cusp, which indicates an optimal design parameter for maximizing fracture toughness density.

The failure mechanism transition is governed by only two parameters, the strength ratio, (σ_1^f/σ_0^f), and θ. An increase in strength ratio gives a transition in tensile failure mechanism at a smaller θ, as shown in Fig. 15e. The effective tensile fracture toughness is a function of the strength ratio and the stiffness ratio. A decrease in strength ratio or an increase in stiffness ratio gives an increase in the non-dimensional tensile fracture toughness, as shown in Fig. 15f and g. The rectangular and trapezoidal suture interfaces are more likely to fracture by interface failure, whereas the anti-trapezoidal suture interface is more likely to fracture by tooth breakage. Fig. 15d shows that the value of θ corresponding to the failure mechanism transition decreases when β increases, and for relatively large θ, suture interfaces of all shapes fail by interface failure.

Additionally, although anti-trapezoidal shapes show the lowest stiffness, strength and fracture toughness among all general trapezoidal shapes, anti-trapezoidal shapes have an advantage over other shapes. The interlocking of anti-trapezoidal teeth is beneficial because interface failure of anti-trapezoidal suture interfaces will not lead to catastrophic failure of the suture interfaces, while for the other three types, interface failure is fatal. This advantage becomes more superior when θ is large and the differences in stiffness, strength and fracture toughness due to geometry are diminishing.

5.2. Shear

Schematics of the two failure mechanisms of the four types of general trapezoidal suture interfaces under shear are shown in Fig. 16a. The predicted stiffness, strength and fracture toughness of the four general trapezoidal suture interfaces under simple shear are shown in Fig. 16b, c and d, respectively. Fig. 16b–d shows that when θ is in the middle range, the stiffness, strength and fracture toughness dependence on geometry is the greatest. However, when θ is very small, the geometry dependence is much smaller.

For almost the entire range of θ, the shear stiffness, strength and fracture toughness follow the ranking of triangular > trapezoidal > rectangular > anti-trapezoidal, as shown in Fig. 16b–d. Fig. 16b–d shows that for all shapes,

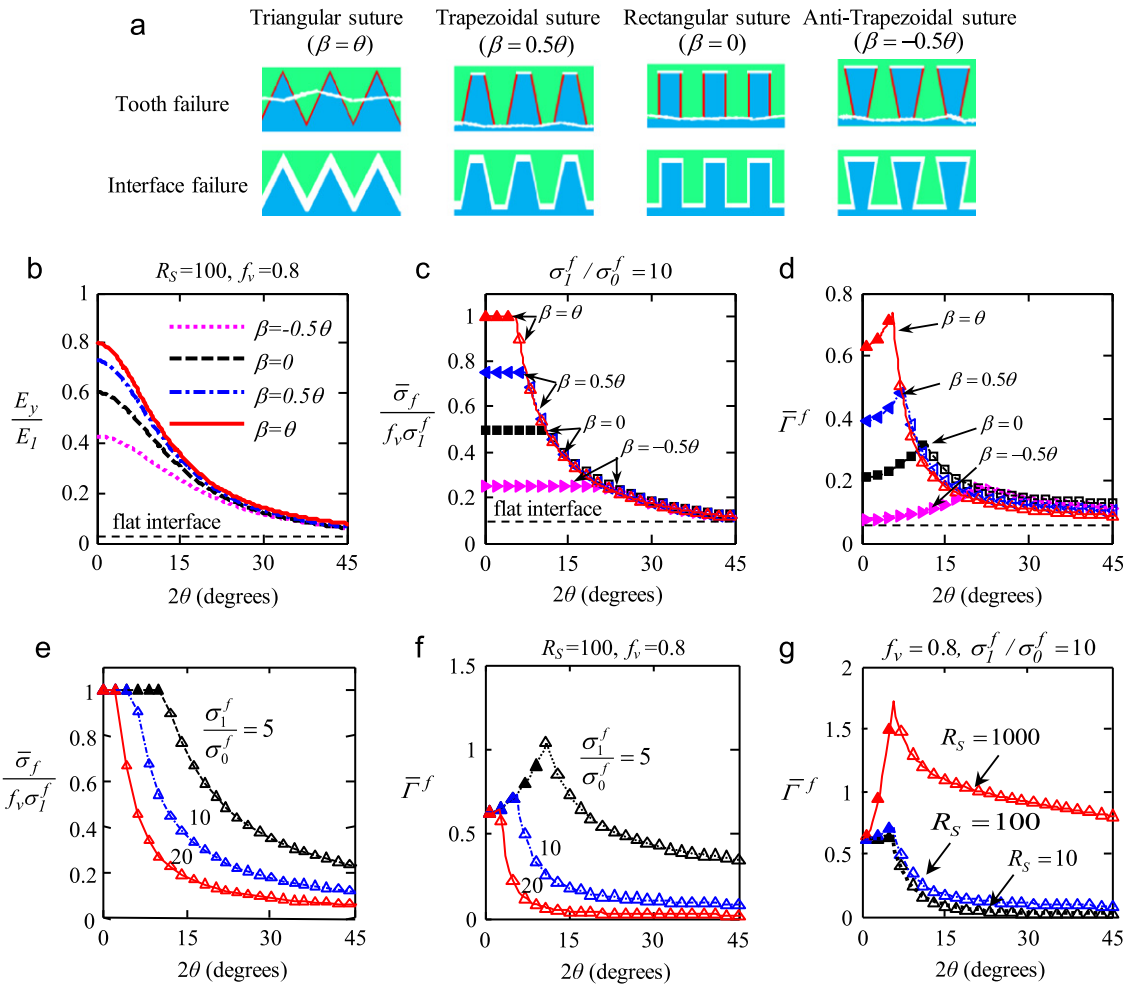

Fig. 15. Mechanical properties of four types of general trapezoidal suture interfaces under longitudinal tension (in (b), (c) and (d), the solid symbols '▲', '◀', '■' and '▶' represent the tooth breakage mechanisms of triangular, trapezoidal, rectangular and anti-trapezoidal suture interfaces respectively; the hollow symbols 'Δ', '◁', '□', and '▷' represent the interface failure mechanisms of triangular, trapezoidal, rectangular and anti-trapezoidal suture interfaces respectively (in (e), (f) and (g), the solid symbols '▲' and the hollow symbols 'Δ' represent the mechanisms of tooth breakage and interface failure respectively). (a) Schematics of two failure mechanisms, (b) nondimensional effective tensile stiffness, (c) strength and (d) fracture toughness as a function of 2θ and β, (e) nondimensional effective tensile strength ($\beta=\theta$) as a function of 2θ and strength ratio, (f) nondimensional effective tensile fracture toughness ($\beta=\theta$) as a function of 2θ and strength ratio, and (g) nondimensional effective tensile fracture toughness ($\beta=\theta$) as a function of 2θ and stiffness ratio.

the shear stiffness strength and fracture toughness show maximum values when the value of θ is in the middle range, and the θ corresponding to a maximum decreases when β increases. Fig. 16d and e shows that the maximum strength and fracture toughness for all shapes occur at the point of failure mechanism transition.

By comparing Figs. 15d and 16d, it can be seen that for the same strength ratio (σ_1^f/σ_0^f), suture interfaces of all shapes have lower shear resistance than tensile resistance and are more likely to fail by tooth breakage under shear than tension.

Again, the failure mechanism transition under shear is governed by two parameters, the strength ratio (σ_1^f/σ_0^f) and θ. A higher strength ratio corresponds to a shear failure mechanism transition at smaller θ, as shown in Fig. 16e. The effective shear fracture toughness is a function of the strength ratio and the stiffness ratio. A decrease in strength ratio or an increase in stiffness ratio gives an increase in the non-dimensional shear fracture toughness, as shown in Fig. 16f and g.

Furthermore, although when θ is large, the anti-trapezoidal shape gains tensile strength due to interlocking without sacrificing tensile and shear stiffness, the shear strength and fracture toughness are sacrificed significantly.

6. Conclusions and discussion

Nature, through the evolutionary process, employs both "inherent" material properties and geometry to produce mechanically functional designs (e.g. Gao, 2006; Ortiz and Boyce, 2008; Garcia et al., 2011; Espinosa et al., 2011). Constraints such as limited availability of materials and energetic costs for fabrication together with the desired functional

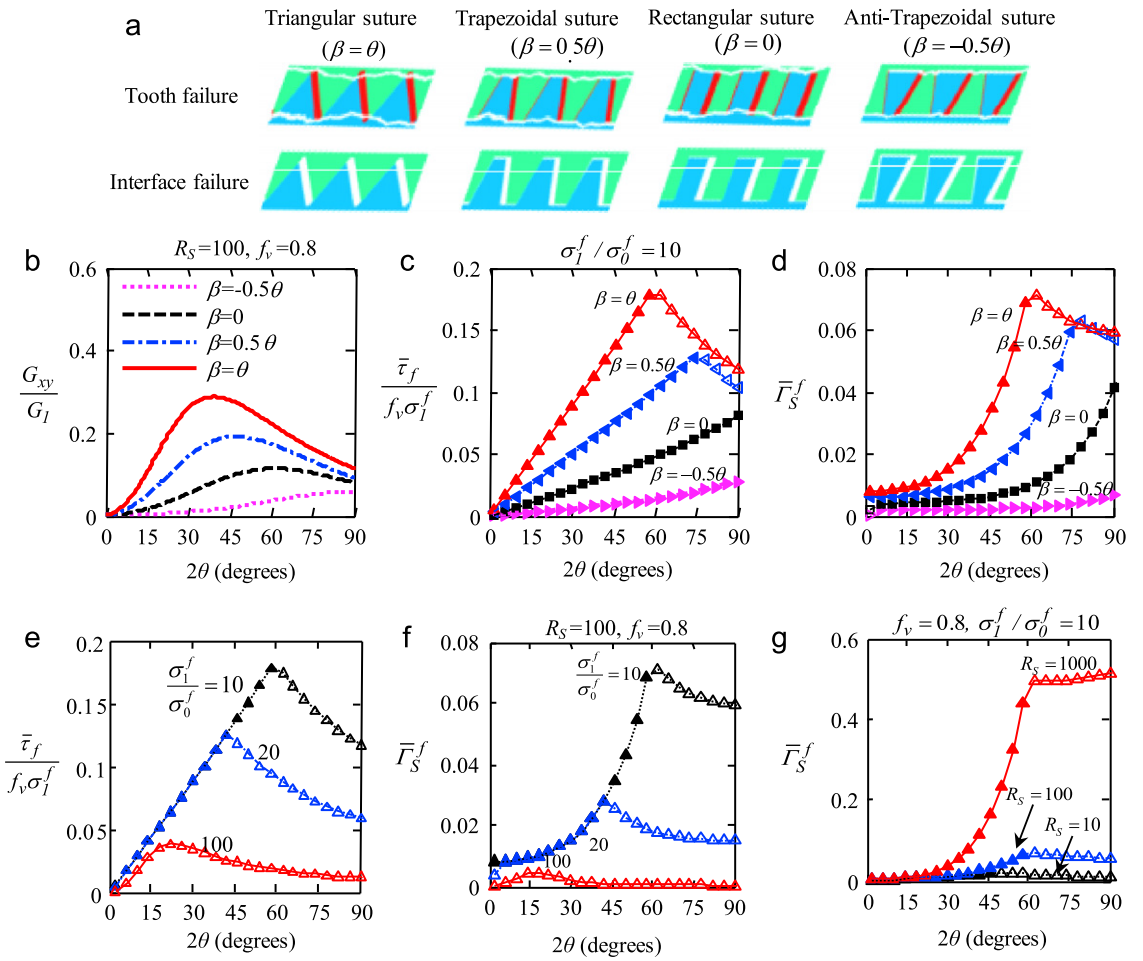

Fig. 16. Mechanical properties of four types of general trapezoidal suture interfaces under simple shear(in (b), (c) and (d), the solid symbols '△', '◁', '■' and '►' represent the tooth breakage mechanisms of triangular, trapezoidal, rectangular and anti-trapezoidal suture interfaces respectively; the hollow symbols 'Δ', '◁', '□', and '▷' represent the interface failure mechanisms of triangular, trapezoidal, rectangular and anti-trapezoidal suture interfaces respectively; in (e), (f) and (g), the solid symbols '▲' and the hollow symbols 'Δ' represent the mechanisms of tooth breakage and interface failure respectively) (a) schematics of two failure mechanisms; (b) nondimensional effective shear stiffness, (c) strength, and (d) fracture toughness as a function of 2θ and β; (e) nondimensional effective shear strength ($\beta=\theta$) as a function of 2θ and strength ratio; (f) nondimensional effective shear fracture toughness ($\beta=\theta$) as a function of 2θ and strength ratio; and (g) nondimensional effective shear fracture toughness ($\beta=\theta$) as a function of 2θ and stiffness ratio.

performance govern the tailoring of geometry as an effective design strategy. The evolutionary diversity of morphometry, in particular at macroscopic length scales, has been studied for many years (e.g. Curry, 1987; Wainwright, 2007). Over the past decade, there has been much focus on identifying and understanding the micro- and nanostructural design principles of biomaterials that lead to mechanical property amplification (Ortiz and Boyce, 2008), but evolutionary diversification in material properties is just beginning to be explored (Blackledge, 2011). Detailed quantitative knowledge and a fundamental understanding of material–geometric design coupling and its functional consequences offer opportunities and insights for design of material systems, especially under design and processing constraints (Gao, 2006; Espinosa et al., 2011; Bruet et al., 2008; Li et al., 2011, 2012). Here, we explore this topic by modeling a biomechanical structure found throughout biology, suture interfaces, which employs both material and geometric design. Of particular interest is the role of geometry in tailoring and amplifying mechanical behavior, providing new and advantageous deformation mechanisms, expanding the design space, and yielding insights into the evolutionary origins and functional consequences.

A general linear elastic composite formulation was developed for an arbitrary suture interface under in-plane loading (i.e. longitudinal tension, lateral tension and simple shear) using the principle of complementary virtual work. Based on this formulation, analytical solutions for stiffness, strength, failure mechanisms, and fracture toughness were derived for general trapezoidal suture interfaces characterized by non-dimensional material properties (tensile and shear stiffness ratios (E_1/E_0) (G_1/G_0) and strength ratio of the materials (σ_1^f/σ_0^f) and a set of independent non-dimensional geometric parameters (θ, β and f_v). Finite element simulations further support the results and provide visualization of the stress and strain and corresponding deformation mechanisms.

6.1. Major results

- *Nonlinear sensitivity*: The mechanical properties of the suture systems exhibit a highly nonlinear dependence on geometry. For example, when θ is small ($2\theta < \sim 30^\circ$), the longitudinal stiffness E_y increases dramatically when θ decreases; while when θ is large ($2\theta > \sim 150^\circ$), the lateral stiffness E_x increases dramatically when θ increases, as shown in Fig. 11. Also, when θ is small, the tensile and shear stiffness, strength and fracture toughness are very sensitive to the shape factor β, as shown in Figs. 15 and 16.
- *Anisotropy*: The structural geometry of the suture waveform results in overall anisotropic mechanical properties. The mechanical anisotropy ratios can be tailored over a range of orders of magnitude by selecting the geometric parameters and the material composition of the suture, as shown in Fig. 12. Anisotropy is one goal of design to allow for optimal use of materials when the prevalent loading and functional requirements are directional.
- *Tailorability and amplification*: The stiffness, strength and fracture toughness of an interface with general trapezoidal wave-forms provide significant enhancements in the mechanical properties when compared to a flat interface (Fig. 15), especially for relatively small θ (where θ is determined by the amplitude to wavelength ratio A/λ for any given volume fraction of tooth material, as shown in Eq. (11)).
  Particular findings include:
  - *Stiffness*: For general trapezoidal suture interfaces,[5] the triangular shape shows the highest stiffness compared to the other three waveforms (trapezoidal, rectangular and anti-trapezoidal) in both tension and shear. The anti-trapezoidal waveform exhibits the lowest stiffness due to its smallest net section at the tooth root and the corresponding non-uniform stress distribution in the teeth which significantly reduces the energy storage capability. The rectangular and trapezoidal waveforms exhibit intermediate properties. When the stiffness ratio increases, shape effects diminish more rapidly with increasing θ since all deformation occurs in the interfacial material. For all shapes, the tensile stiffness increases when θ decreases. In contrast, the shear stiffness reaches a peak when θ reaches a critical value θ_S^* (by taking $G_{xy}'=0$, in Eq. (23a), where θ_S^* is strongly dependent on β and the stiffness ratio R_S; θ_S^* decreases with increasing R_S and is smallest for the triangular waveform and largest for the anti-trapezoidal, as shown in Fig. 16b. These shear stiffness dependencies are directly related to the bending and shearing deformation mechanisms of the teeth and corresponding stress distributions which all depend on β.
  - *Strength*: General trapezoidal suture interfaces have two failure mechanisms: tooth breakage and interface failure. Under tension, a critical θ° exists: when $\theta < \theta^\circ$, tooth breakage occurs, and when $\theta > \theta^\circ$, interface failure occurs. When the failure mechanism of tooth breakage occurs, the triangular shape shows the highest strength in both tension and shear due to its uniform stress distribution which provides the most efficient usage of the materials. The anti-trapezoidal suture interface shows the lowest strength due to the smallest net section area of the tooth root giving a large stress concentration which means the macroscopic stress at which the suture fails is lowest for this geometry. The strengths of the rectangular and trapezoidal interfaces lay in between.
    When the failure mechanism is interface failure instead of tooth breakage, the anti-trapezoidal suture interface offers an advantage in tension due to the interlocking between the teeth. Under shear loading, interlocking between teeth occurs for all shapes and thus interface failure under shear does not correspond to catastrophic failure for any of these shapes. For all shapes, the tensile strength increases when θ decreases and is constant after $\theta = \theta^\circ$. In contrast, the shear strength reaches a peak when θ reaches a critical value θ_S^o which is not only strongly dependent on β and the strength ratio (σ_1^f/σ_0^f), but also dependent on the stiffness ratio, as shown in Figs. 15g and 16g.
  - *Fracture toughness*: Fracture toughness of general trapezoidal suture interfaces shows a cusp at the point of failure mechanism transition for both tension (when $\theta=\theta^\circ$, Eq. (25c)) and shear (when $\theta=\theta_S^o$): for $\theta < \theta^\circ$ (tension) or $\theta < \theta_S^o$ (shear), the fracture toughness increases rapidly when θ increases; for $\theta > \theta^\circ$ (tension) or $\theta > \theta_S^o$ (shear), the fracture toughness decreases rapidly when θ increases. Therefore, θ° (tension) and θ_S^o (shear) each provides an optimal geometry which maximizes the fracture toughness. θ° is governed by the strength ratio of the two phases, where an increase in strength ratio gives a smaller θ°, as shown in Fig. 15f, because the suture interfaces will fail by interface failure since the stress levels in the teeth do not reach magnitudes large enough to cause tooth breakage. However, θ° does not depend on the stiffness ratio, while θ_S^o does, as shown in Fig. 16g, where an increase in stiffness ratio gives a larger θ_S^o. Again, when the failure mechanism of tooth breakage occurs, the triangular shape shows the highest fracture toughness over the other three types in both tension and shear. The anti-trapezoidal suture interface shows the lowest fracture toughness, as shown in Figs. 15d and 16d.
- *Optimization*: The triangular tooth geometry shows the optimal longitudinal tensile strength due to the remarkable uniform normal stress distribution in the teeth and uniform shear stress in the interfacial layer (Li et al., 2011). In fact, triangular suture interfaces show the maximum tensile and shear stiffness, strength, and fracture toughness among all general trapezoidal shapes as shown in Figs. 15 and 16. The rectangular geometry exhibits the optimal lateral strength as shown in Fig. 7b. Tensile stiffness for all waveforms increases with decreasing θ. Also, optimal tip angles were found for maximizing the tensile strength (θ^o, Eq. (25c)), the shear strength (θ_S^o) and also the fracture toughness, and were found to be strongly dependent on the mechanical property ratios and the waveform (β). These optimal values are a

[5] The slant segments of interfaces are dominant and the influences of the flat segments of interface are small.

direct result of the stress distribution and strain energy in the different waveforms for the different loading conditions.

- *Advantageous deformation mechanisms*: Generally, non-single valued interfacial profiles normal to the loading condition can provide interlocking mechanisms which resist the loading and can provide a damage tolerance to overall suture failure once interface failure has occurred. For example, the interlocking mechanism of dove-tail shaped building blocks in nacre-inspired composites were demonstrated through experiments, simulations, and a model material in the literature (Barthelat et al., 2007; Tang et al., 2007; Espinosa et al., 2011; Barthelat and Zhu, 2011)). Also, the out-of-plane interlocking mechanism of turtle suture were shown via experiments and analytical modeling (Krauss et al., 2009), and the in-plane interlocking mechanisms of ammonite-inspired hierarchical suture interface were explored analytically via a deterministic fractal model (Li et al., 2012). Furthermore, during shear, all waveform profiles other than flat interface provide interlocking to provide a damage tolerance mechanism for shear loading.
- *Bio-inspired design*: The general formulation of the mechanics of suture interfaces with arbitrary geometry and the specific solutions for general trapezoidal suture interface can serve as a design guideline for engineering systems and synthetic materials. Therefore, suitable shapes and geometric parameters should be chosen to reach the optimal mechanical function under different loading cases:
  - To resist uniaxial tension/compression, a triangular shape with small θ is recommended. Triangular shape with large θ needs to be avoided because of the significantly reduced tensile stiffness, strength and fracture toughness when θ increases.
  - To resist multi-axial tension/compression, anti-trapezoidal or triangular shape with relatively large θ ($\sim 45^\circ$) is recommended in order to provide isotropy. Also, because the anti-trapezoidal shape gains provide the interlocking mechanism for all loading, these shapes are desirable for interfaces which will be subjected to multiaxial loading even though its shear strength and fracture toughness are lowest. In fact, any interface profile $f(x)$ of non-single valued function will show a similar interlocking effect.
  - To resist shear, triangular shapes with θ in the middle range (15–45°) are recommended because of the peak stiffness, strength and fracture toughness in this range. Triangular shapes with small θ needs to be avoided because of the significantly reduced shear stiffness, strength and fracture toughness which arise due to the bending of the teeth during shear. The anti-trapezoidal shape is not recommended for resisting shear due to the significantly reduced shear strength and fracture toughness.
  - Anti-trapezoidal shape is recommended to avoid catastrophic failure and provides damage tolerance when θ must be large and good adhesives are not available.

6.2. Relevance to biological systems

Interestingly, suture interfaces in natural systems follow the aforementioned rules in tailoring geometry. For example, the pelvic suture of *Gasterosteus aculeatus* (three-spined stickleback) is mainly under uniaxial tension/compression loading when fulfilling daily function (Song, 2011; Song et al., in review), thus triangular suture interfaces are employed and show a spatial variation in θ corresponding to spatially distributed loading levels, with small θ in the region where high stiffness is required and large θ in the region where low stiffness is needed (Song et al., in review; Song, 2011). Diatom suture interfaces connecting two neighboring frustules (where the frustules have a cylindrical shape) are under bi-axial tension/compression and in-plane shear, therefore, general trapezoidal shapes are employed with a θ value in the middle range and θ is uniform due to the axial symmetry of the cylindrical frustules generating the nature of the loading. The cranial suture of vertebrates are under multi-axial tension/compression due to the irregular spherical shape of the skull, thus the cranial sutures exhibit a very complicated shape with tooth in various shapes growing in different directions, as shown in Fig. 1f.

In conclusion, the general suture interface model captures the dependence of the mechanical behavior including stiffness, strength and deformation and failure mechanisms of the suture interface on the geometry and material composition. This model can be used to derive detailed guidelines for designing the geometry and choosing material composition of suture interface to function under different in-plane loading cases and also provides insights into the morphological diversity of suture interfaces in biological systems.

Acknowledgments

We gratefully acknowledge support of the US Army through the MIT Institute for Soldier Nanotechnologies (ISN)—Institute for Collaborative Biotechnologies (ICB) at University of California at Santa Barbara (UCSB) (Contract DAAD-19-02-D0002), and the National Security Science and Engineering Faculty Fellowship Program (N00244-09-1–0064).

Appendix A. Derivation of stress distribution in the teeth of general trapezoidal suture interfaces

Force equilibrium yields the relationship between the normal stress within the tooth, $\sigma_{yy}(y)$, and the interfacial normal and tangential traction, $\tau_n(y)$ and $\tau_t(y)$

$$[\sigma_{yy}(y)+dS][f(y)+df]-\sigma_{yy}(y)f(y)=\tau_t\frac{dx}{\cos\beta}\cos\beta+\tau_n\frac{dx}{\cos\beta}\sin\beta. \tag{A1}$$

By neglecting the higher order term, we have

$$d[\sigma_{yy}(y)f(y)]=(\tau_t+\tau_n\tan\beta)\,dy. \tag{A2}$$

By using Eqs. (19), Eq. (A2) becomes

$$\frac{d[\sigma_{yy}(y)f(y)]}{dy}=\sigma_y\tan\varphi. \tag{A3}$$

Due to the boundary conditions that $\sigma_{yy}(0)=0$, and $\sigma_{yy}(A)=\sigma_y$, the stress distribution in the teeth is obtained

$$\sigma_{yy}(y)=\frac{\sigma_y y\tan\varphi}{y\tan\beta+A(\tan\varphi-\tan\beta)}. \tag{A4}$$

Hence, the elastic energy stored in the teeth $\mathcal{E}$ is expressed as

$$\mathcal{E}=\int_0^A\frac{\sigma_{yy}(y)^2}{E_1}w(y)\,dy=\int_0^1 U(y)\,d\frac{y}{A}, \tag{A5}$$

where $U(y)$ is the strain energy density per unit length along the teeth amplitude. $U(y)$ is normalized by $U_0=\sigma_y^2A^2$ as

$$\frac{U(y)}{U_0}=\frac{\sigma_{yy}(y)^2}{\sigma_y^2A^2}\frac{w(y)}{A}. \tag{A6}$$

Eqs. (A4) and (A6) are plotted in Fig. A1, showing the consistency between the analytical results and the numerical results from finite element simulaitons.

Therefore, the function in Eq. (20a)–(20c) is obtained

$$\zeta(\beta,\varphi)=\frac{2\mathcal{E}E_1f_v^2}{\overline{\sigma}_y{}^2}. \tag{A7}$$

By substituting Eq. (A5) into Eq. (A7), Eqs. (20b) and (20c) are derived.

Appendix B. Boundary and loading conditions of the RVEs of general trapezoidal sutures

Generally, for an arbitrary loading case, a macroscopic displacement gradient **H** is imposed to the field of a RVE (Figs. B1 and B2) via periodic boundary conditions (Danielsson et al., 2002), where $\mathbf{H}=\mathbf{F}-\mathbf{I}$, **F** is the deformation gradient, and **I** is a unit tensor. The periodicity of suture interface is only along *x*-direction.

Specifically, there are two cases corresponding to two different RVE boundaries:

1. With flat tip material
   The RVE has boundaries A–B–C–D (Fig. B1). Only the edges of AD and BC need to satisfy the periodic boundary conditions. By definition, the relative displacement of nodes on AD and BC, $\mathbf{u}|_{\mathbf{AD}}-\mathbf{u}|_{\mathbf{BC}}=\mathbf{HL}$, where, the displacement

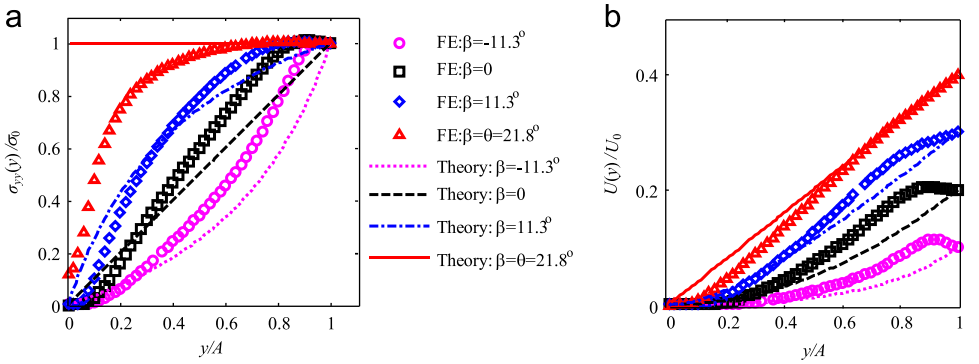

Fig. A1. Stress distribution (a) and distribution of strain energy density per unit length (b) along the teeth for four types of trapezoidal suture interfaces.

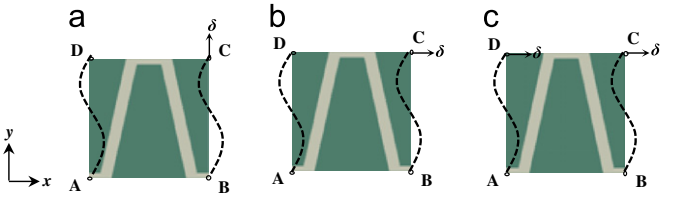

Fig. B1. Schematics of the loading and boundary conditions in finite element simulations of a RVE of general trapezoidal sutures with tip materials, for (a) longitudinal tension, (b) lateral tension, and (c) simple shear.

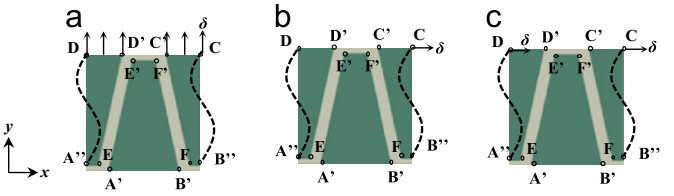

Fig. B2. Schematics of the loading and boundary conditions in finite element simulations of a RVE of general trapezoidal sutures with no materials at the flat tips, for (a) longitudinal tension, (b) lateral tension, and (c) simple shear.

vector of a node is $\mathbf{u}=(u_x, u_y)'$, and the length of AB and AD in the reference coordinates, $\mathbf{L}=[(X_B-X_A), (Y_D-Y_A)]'$, and

$$\mathbf{H}=\begin{bmatrix} H_{11} & H_{12} \\ H_{21} & H_{22} \end{bmatrix}.$$

For longitudinal tension

$$\mathbf{H}=\begin{bmatrix} \bar{\varepsilon}_x & 0 \\ 0 & 0 \end{bmatrix},$$

and the prescribed displacements are $\mathbf{u_A}=(0,0)$, all other nodes on AB have displacements $\mathbf{u_{A'B'}}=$(free, 0), and all nodes on CD have displacements $\mathbf{u_{CD}}=$(free, δ); for lateral tension

$$\mathbf{H}=\begin{bmatrix} 0 & 0 \\ 0 & \bar{\varepsilon}_y \end{bmatrix},$$

and the prescribed displacements are $\mathbf{u_A}=(0, 0)$, $\mathbf{u_D}=(0,$ free), $\mathbf{u_C}=(\delta,$ free), all other nodes on AB (except A) have displacements $\mathbf{u_{AB}}=$(free, 0), and the u_x of the nodes on CD are the same; for simple shear

$$\mathbf{H}=\begin{bmatrix} 0 & \bar{\gamma}_{xy} \\ 0 & 0 \end{bmatrix},$$

and the prescribed displacements of the nodes on the boundaries are that all nodes on AB have displacements $\mathbf{u_{AB}}=(0, 0)$, and all the nodes on DD' and CC' have displacements $\mathbf{u_{CD}}=(\delta, 0)$, as shown in Fig. B1.

2. No material at the flat tips
The RVE has boundaries A"–E–A'–B'–F–B"–C–C'–F'–E'–D'–D (Fig. B2), i.e. has nodes on these boundaries (for example, there are no nodes on A"A and AA'). Only the nodes on the edges of A"D and B"C need to satisfy the periodic boundary conditions. By definition, the relative displacement of nodes on A"D and B"C, $\mathbf{u}|_{\mathbf{A"D}}-\mathbf{u}|_{\mathbf{B"C}}=\mathbf{HL}$, where, the length of A"B" and A"D in the reference coordinates, $\mathbf{L}=[(X_{B"}-X_{A"}), (Y_D-Y_{A"})]'$. The components of $\mathbf{H}$ are the same as case (1) for the three loading cases. As for the prescribed displacements: for longitudinal tension, the prescribed displacements are $\mathbf{u_{A'}}=(0,0)$, all other nodes on A'B' have displacements $\mathbf{u_{A'B'}}=$(free, 0), all nodes on DD' and C'C have displacements $\mathbf{u_{DD'}}=\mathbf{u_{CC'}}=$(free, δ); for lateral tension, the prescribed displacements are $\mathbf{u_{A"}}=(0,0)$, $\mathbf{u_D}=(0,$ free), $\mathbf{u_C}=(\delta,$ free), $\mathbf{u_{B"}}=$(free, 0), the u_x of the nodes on A'B' are the same, and the u_x of the nodes on DD' and C'C are the same; for simple shear, nodes on A'B' have displacements $\mathbf{u_{A'B'}}=(0, 0)$, and all the nodes on DD' and CC' have displacements $\mathbf{u_{DD'}}=\mathbf{u_{CC'}}=(\delta, 0)$, as shown in Fig. B2. For all three loading cases, all nodes on E'F' and all other nodes (not prescribed as above) on A"E, FB" are free.

Appendix C. Initial stiffness for general trapezoidal sutures with flat tip interface

Finite element simulations were conducted for the models of general trapezoidal suture interfaces with flat tip materials with $\theta=21.8^\circ$, and $\beta=21.8^\circ$, 11.3°, 0° and -11.3°, (for triangular, trapezoidal, rectangular and anti-trapezoidal sutures, respectively). The initial lateral and longitudinal tensile stiffness *Ex* and *Ey* of these models were obtained from

Table C1
Comparison of the FE simulation results of general trapezoidal suture interfaces with and without tip material.

E_y (MPa)	$R_S=10$		$R_S=100$		$R_S=1000$		$R_S=10{,}000$	
	With tip	No tip	With tip	No tip	With tip	No tip	With tip	No tip
Anti-trapezoidal	9998.0	2300.8	2848.8	580.0	347.9	68.8	35.7	7.0
Rectangular	7207.4	2985.6	2057.2	584.0	246.5	64.8	25.1	6.5
Trapezoidal	9832.0	3656.8	1711.7	639.2	179.3	68.8	18.1	7.0
Triangular	8159.0	4448.0	1626.6	768.0	183.9	83.2	19.2	8.3

these simulations. These stiffnesses were compared with those without tip material. *Ex* of the two types of models (with and without tip materials) are nearly the same, i.e. the material at the flat tip has little influence on the lateral tensile stiffness. However, the material at the flat tip increases the initial longitudinal stiffness (*Ey*) significantly, as shown in the table below, (E_1 is fixed as 10,000 MPa for all simulations, $Rs=E_1/E_0$) (Table C1).

Appendix D. Derivation of shear stiffness of general trapezoidal suture interfaces

For the general trapezoidal suture interfaces, the external complementary virtual work of far-field virtual tangential traction $\delta\overline{\sigma}_{xy}$ is

$$\delta W_e^* = \Delta\delta\overline{\sigma}_{xy}\lambda, \tag{D1}$$

where Δ (refer to Fig. 8a) is the tooth displacement at the boundary due to $\delta\overline{\sigma}_{xy}$ and is related to $\delta\overline{\sigma}_{xy}$ and the effective shear modulus of suture interface G_{xy} as, $\Delta=(\delta\overline{\sigma}_{xy}A/G_{xy})$, where A is the wave amplitude.

The variational strain energy including the deformation of teeth is expressed as

$$\delta U^* = \int_{V_0}\left(\frac{\tau_t}{G_0}\delta\tau_s+\frac{\tau_n}{E_0^{PS}}\delta\tau_n\right)dV_0+\int_0^A\left[\frac{M(y)}{E_1I}\delta M(y)+\frac{N(y)}{G_sA_s}\delta N(y)\right]\lambda\,dy, \tag{D2}$$

where $\delta M=EIv''$, $\delta N=G_sA_sv'$. We can see that the deformation energy of the teeth has two components: bending and shear. The deflection of the equivalent beam can be solved via the following governing equations considering the coupling between shear and bending:

$$\begin{cases} G_sA_s(v'-v_b')=E_1Iv_b''' \\ E_1Iv_b'''=\delta\overline{\sigma}_{xy}(\lambda-2g) \end{cases}. \tag{D3}$$

where E_1 is Young's modulus of tooth material; I is the moment of inertia of the cantilever beam, $I=1/12(\lambda-2g)^3$; A_s is the effective shear area of the cross section, and for a rectangular cross section, $A_s=(2/3)(\lambda-2g)$; G_s is the local shear modulus (shown in Fig. 8b), which is calculated by the Voigt law as $G_s=G_0(1-f_v)+G_1f_v$. Therefore, the total deflection along the tooth is solved as a polynomial function as

$$v(x)=\delta\overline{\sigma}_{xy}\lambda\left[\frac{x^3}{6E_1I}+\frac{Ax^2}{2E_1I}+\frac{x}{G_sA_s}\right] \tag{D4}$$

and the deflection due to bending is

$$v_b(x)=\delta\overline{\sigma}_{xy}\lambda\left[\frac{x^3}{6E_1I}+\frac{Ax^2}{2E_1I}\right]. \tag{D5}$$

If we assume the teeth are rigid, the kinematics of the interface yields the relation between $\delta\tau_n$ and Δ, $\delta\tau_t$ and Δ: $\delta\tau_t=(\Delta/g)G_0\tan\beta$, and $\delta\tau_n=(\Delta/g)E_0^{PS}$. If we assume the teeth are deformable

$$\delta\tau_s=G_0\left[\frac{(\Delta-\Delta_b)}{g}\tan\beta-\gamma_b\right], \tag{D6}$$

and $\delta\tau_n=E_0^{PS}((\Delta-\Delta_b)/g)$, where Δ_b is a representative deflection of a tooth due to bending deformation due to $\delta\overline{\sigma}_{xy}$, and γ_b is the corresponding shearing deformation. The representative deformation of the tooth is evaluated in the middle of the equivalent beam as, $\Delta_b=v(A/2)$, and $\gamma_b=v'(A/2)$. For relatively small θ, due to shear and bending of the teeth, the contribution to overall deformation from the teeth is significant. Thus by substituting Eqs. (21), (22), (D1), (D2), and (D3) into Eq. (4), Eq. (23a) can be derived.

References

Barthelat, F., Tang, H., Zavattieri, P.D., Li, C.M., Espinosa, H.D., 2007. On the mechanics of mother-of-pearl: a key feature in the material hierarchical structure. J. Mech. Phys. Solids 55 (2), 306–337.
Blackledge, T.A., 2011. Prey capture in orb weaving spiders: are we using the best metric? J. Arachnol. 39, 205–210.
Bruet, B.J.F., Song, J.H., Boyce, M.C., Ortiz, C., 2008. Materials design principles of ancient fish armour. Nat. Mater. 7 (9), 748–756.

Curry R.L., 1987. Evolution and Ecology of Cooperative Breeding in Galapagos Mockingbirds (Nesomimus spp.). Ph.D. Thesis. University of Michigan, Ann Arbor.
Daniel, T.L., Helmuth, B.S., Saunders, W.B., Ward, P.D., 1997. Septal complexity in ammonoid cephalopods increased mechanical risk and limited depth. Paleobiology 23 (4), 470–481.
Danielsson, M., Parks, D.M., Boyce, M.C., 2002. Three-dimensional micromechanical modeling of voided polymeric materials. J. Mech. Phys. Solids 50, 351–379.
De Blasio, F.V., 2008. The role of suture complexity in diminishing strain and stress in ammonoid phragmocones. Lethaia, 15–2441, 15–24.
Dunlop, J.W.C., Weikamer, R., Fratzl, P., 2011. Artful interfaces within biological materials. Mater. Today 14 (3), 70–78.
Espinosa, H.D., Juster, A.L., Latourte, F.J., Loh, O.Y., Gregoire, D., Zavattieri, P.D., 2011. Tablet-level origin of toughening in abalone shells and translation to synthetic composite materials. Nat. Commun. 2, Article number 173. http://dx.doi.org/10.1038/ncomms1172.
Gao, H.J., 2006. Application of fracture mechanics concepts to hierarchical biomechanics of bone and bone-like materials. Int. J. Fracture 138 (1-4), 101–137.
Garcia, A.P., Pugno, N., Buehler, M.J., 2011. Superductile, wavy silica nanostructures inspired by diatom algae. Adv. Biomater. 13 (10), B405–B414.
Gebeshuber, I.C., Kindt, J.H., Thompson, J.B., Del Ano, Y., Stachelberger, H., Brzezinski, M.A., Stucky, G.D., Morse, D.E., Hansma, P.K., 2003. Atomic force microscopy study of living diatoms in ambient conditions. J. Microsc., 292–299212, 292–299.
Hassan, M.A., et al., 2002. Finite-element analysis of simulated ammonoid septa (extinct Cephalopoda): septal and sutural complexities do not reduce strength. Paleobiology 28 (1), 113–126.
Herring, S.W., 2008. Mechanical influences on suture development and patency. Front. Oral. Biol. 12, 41–56.
Hubbard, R.P., Melvin, J.W., Barodawa, I.T., 1971. Flexure of cranial sutures. J. Biomech. 4 (6), 491–496.
Jasinoski, S.C., et al., 2010. Mechanics of cranial sutures using the finite element method. J. Biomech. 43 (16), 3104.
Jaslow, C.R., 1990. Mechanical properties of cranial sutures. J. Biomech. 23 (4), 313–321.
Ji, B.H., Gao, H.J., 2004. Mechanical properties of nanostructure of biological materials. J. Mech. Phys. Solids 52. 1963–1990.
Krauss, S., et al., 2009. Mechanical function of a complex three-dimensional suture joining the bony elements in the shell of the red-eared slider turtle. Adv. Mater. 21 (4), 407–412.
Li, Y.N., Ortiz, C., Boyce, M., 2011. Stiffness and strength of suture joints in nature. Phys. Rev. E 84, 062904.
Li, Y.N., Ortiz, C., Boyce, M., 2012. A bio-inspired mechanical, deterministic fractal model for hierarchical suture joints. Phys. Rev. E 85, 03190.
Lin, E., Li, Y.N., Ortiz, C., Boyce, M. C. Deformation and failure mechanisms of general trapezoidal suture interfaces, in preparation.
Long, C.A., Long, J.E., 1992. Fractal dimensions of cranial sutures and waveforms. Acta Anat. (Basel) 145, 201–206.
Moazen, M., et al., 2009. Assessment of the role of sutures in a lizard skull: a computer modeling study. Proc. R. Soc. B, 39–46. 276.
Ortiz, C., Boyce., M.C., 2008. Bioinspired structural materials. Science 319 (5866), 1053–1054.
Persson, M., Magnusson, B.C., Thilander, B., 1978. Sutural closure in rabbit and man: a morphological and histochemical study. J. Anat. 125, 313–321.
Potapova, M., English, J. (2010). Aulacoseira ambigua. In: Diatoms of the United States. Retrieved October 29, 2011, from 〈http://westerndiatoms.colorado.edu/taxa/species/aulacoseira_ambigua〉.
Pritchard, J.J., Scott, J.H., Girgis, F.G., 1956. The structure and development of cranial and facial sutures. J. Anat. 90, 73–86.
Saunders, W.B., Work, D.M., Nikolaeva, S.V., 1999. Evolution of complexity in Paleozoic ammonoid sutures. Science, 760–763286, 760–763.
Song, J.H., et al., 2010. Quantitative microstructural studies of the armor of the marine three-spine stickleback (*Gasterosteus aculeatus*). J. Struct. Biol. 171 (3), 318–331.
Song J., Li, Y.N., Lin, E., Wund, M., Araya, S., Boyce, M., Ortiz, C. Functional diversity and dynamic biomechanical mechanisms of the three-spine stickleback armor, in review.
Song J., 2011. Multiscale materials design of natural exoskeletons. Ph.D thesis, MIT.
Spaulding, S., Edlund, M., Metzeltin, D., 2009. Fallacia. In: Diatoms of the United States. Retrieved October 29, 2011, from 〈http://westerndiatoms.colorado.edu/taxa/genus/Fallacia〉.
Tang, H., Barthelat, F., Espinosa, H.D., 2007. An elasto-viscoplastic interface model for investigating the constitutive behavior of nacre. J. Mech. Phys. Solids 55 (7), 1410–1438.
Wainwright, P.C., 2007. Functional versus morphological diversity in macroevolution. Annu. Rev. Ecol. Evol. Syst. 38, 381–401.
Barthelat, F., Zhu, D., 2011. A novel biomimetic material duplicating the structure and mechanics of natural nacre. J. Mater. Res. 26 (10), 1–13.